

**Estimation of lost electrons and muons
from $t\bar{t}$ and W^\pm +jets events
at the CMS detector**

Diplomarbeit

**Institute für Experimentalphysik
der Universität Hamburg**

vorgelegt von

Arne-Rasmus Dräger

Hamburg

2012

Gutachter der Doktorarbeit: Prof. Dr. Christian Sander

Abstract

The LHC has collected 4.98 fb^{-1} of proton-proton collisions at a center of mass energy of 7 TeV. A search for physics beyond the Standard Model with high energetic jets and large missing transverse energy takes advantage of this data. The background from Standard Model processes is estimated to a high precision using data-driven estimation methods. The prediction of the Standard Model background arising from $t\bar{t}$ and W^\pm +jets events with unidentified electrons and muons from the involved W^\pm -decay is presented in this thesis.

No excess above Standard Model expectation could be found. The results are interpreted within the minimal supersymmetric Standard Model and for Simplified Models excluding squark and gluino masses up to $\tilde{q} \approx 1.2 \text{ GeV}$ and $\tilde{g} \approx 650 \text{ GeV}$.

Abriss

Der LHC hat 4.98 fb^{-1} von Proton-Proton Kollisionen bei einer Schwerpunktsenergie von 7 TeV aufgezeichnet. Eine Suche nach Physik jenseits des Standard Modells, mit hoch energetischen Jets und viel fehlender transversaler Energie, wird in dieser Arbeit beschrieben. Untergrund von Standard Model Ereignissen wird mit einer hohen Präzision Daten-Getrieben vorher gesagt. Diese Arbeit beschreibt die Vorhersage von nicht detektierten Muonen und Elektronen aus $t\bar{t}$ und $W^{\pm} + \text{jets}$ Zerfällen.

Es wird kein Überschuss an Ereignissen gegenüber den vom Standard Modell erwarteten Ereignissen beobachtet. Das Resultat wird in dem minimal supersymmetric Standard Model und Simplified Models interpretiert. Massen von squark und gluino Massen unterhalb $\tilde{q} \approx 1.2 \text{ GeV}$ und $\tilde{g} \approx 650 \text{ GeV}$ können ausgeschlossen werden.

Contents

1	Introduction	4
2	Theory	5
2.1	Standard Model	5
2.1.1	The Dirac equation and gauge groups	5
2.1.2	Quantum Electrodynamics (QED)	6
2.1.3	The weak force and the electroweak unification	7
2.1.4	QCD	8
2.1.5	The Higgs Mechanism	9
2.2	Open questions and problems of the SM	10
2.3	Supersymmetry	11
2.3.1	SUSY breaking in the Model of Minimal Supergravity and the cMSSM	12
3	LHC and CMS detector	13
3.1	The Large Hadron Collider (LHC)	13
3.2	The Compact Muon Solenoid detector	15
3.2.1	The tracker	17
3.2.2	The Electromagnetic Calorimeter	17
3.2.3	The Hadronic Calorimeter	18
3.2.4	The Solenoid and the Muon Chambers	19
3.2.5	Trigger	19
3.3	Particle identification and physical object definitions	20
3.4	The particle-flow algorithm	21
4	The concept of jets with missing transverse momentum analysis	23
4.1	Event Selection	24
4.2	Regions of Interest	25
4.3	Data and simulated event samples	25
5	The prediction of lost leptons from $t\bar{t}$ and W^\pm+jets events	28
5.1	Concept of the lost-lepton background estimation	28
5.2	The control sample	29
5.2.1	Signal Contamination	31
5.2.2	Other SM background contributions	32
5.3	Predicting the lost electrons and muons	34
5.4	Lepton Efficiencies	36
5.4.1	Tag&Probe method	36
5.4.2	Leptons out of the detector acceptance	36
5.4.3	Not reconstructed leptons	37
5.4.4	Not isolated leptons	40

5.5	Closure tests and prediction on data	42
5.6	Pileup dependency studies	51
5.7	PDF uncertainties on the acceptance	55
5.8	Uncertainties	56
6	Combination of other backgrounds with the lost lepton and result interpretation	59
6.0.1	The QCD background estimation	59
6.0.2	The Z to invisible background estimation	61
6.0.3	The hadronic τ background estimation	61
6.1	Combination of all backgrounds	62
6.2	Interpretation of the results	65
6.2.1	Interpretation within the cMSSM	65
6.2.2	Interpretation with Simplified Model Spectra	67
7	Conclusion and outlook	69
8	Appendix	70
	Bibliography	72

List of Figures

2.1	This figure contains fermions and gauge bosons of the SM. The Higgs boson is not included since its existents has still not been verified by experiments.	6
3.1	An exploded view of the CMS detector.	13
3.2	An exploded view of the CMS detector.	15
3.3	An exploded view of the CMS detector.	17
3.4	This figure shows the transverse slice through the CMS detector with typical particle interaction signatures with the detector.	22
5.1	Feynman diagram for a typical W^\pm +jets decay on the left and a $t\bar{t}$ decay on the right at the LHC [1].	28
5.2	This plot shows a comparison of the μ control sample p_T spectrum selected on data corresponding to the full 4.98 fb $^{-1}$ recorded 2011 and simulated $t\bar{t}$ and W^\pm +jets events referred to as MC.	29
5.3	These figures show a comparison of the μ control sample for the H_T and \cancel{H}_T distribution selected on data corresponding to the full 4.98 fb $^{-1}$ recorded 2011 and simulated $t\bar{t}$ and W^\pm +jets events.	30
5.4	This plot shows the m_T distribution of the control sample in data, for simulated $t\bar{t}$ and W^\pm +jets events and for an example signal point (LM5). The m_T distribution of the CS steeply falls above 80 GeV for the SM process, where as the LM5 distribution is rather wide. (The legend description can be found in the caption of Fig. 5.2)	31
5.5	This plot shows the efficiency of the m_T cut for all exclusive regions (the numbering corresponds to the enumeration in Tab.4.1) for bin 1-14. Bin 16 shows the value for the baseline selection.	33
5.6	Visualization of the steps a muon has to take in order to enter the control sample	34
5.7	These plots show the MC closure ($t\bar{t}$ and W^\pm +jets combined) for not reconstructed electrons (upper two plots) and muons (lower two plots). On the left side for the old efficiencies binned in $\frac{p_{t,lep}}{p_{t,jet}}$ and η and on the right side with the new in lepton p_T and ΔR binned efficiencies.	38
5.8	These plots show the electron and μ reconstruction efficiencies obtained from MC.	39
5.9	These plots show the electron and μ isolation efficiencies calculated with a Tag&Probe method.	41
5.10	These plots show the closure test for the H_T and \cancel{H}_T baseline selection for the total lost-lepton background. The estimated lost-leptons are called Data-driven Prediction from MC, which refers to $t\bar{t}$ and W^\pm +jets events combined and the observed lost-leptons are referred to as MC expectation.	44

5.11	Comparison of the prediction on data vs. the prediction on MC ($t\bar{t}$ and W^\pm +jets combined) for the H_T (on the right) and the \cancel{H}_T (on the left) distribution. For the data prediction all uncertainties are shown while for the MC prediction only statistical uncertainties are shown. The shapes agree well within the uncertainties.	45
5.12	This plots show the closure test of the Data-driven Prediction from MC and the MC expectation for the H_T and \cancel{H}_T distribution for $t\bar{t}$ simulated events. Good agreement of the shape as well as the ratio can be seen. Only the \cancel{H}_T distribution shows a significant discrepancy.	46
5.13	This plots show the closure test of the Data-driven Prediction from MC and the MC expectation for the H_T and \cancel{H}_T distribution for W^\pm +jets simulated events. Good agreement of the shape as well as the ratio can be seen. . . .	47
5.14	This plots show the closure tests for $t\bar{t}$ events separated for the not isolated (top), not reconstructed (middle) and out of acceptance fraction (bottom). Good agreement for the shape can be observed. However, an increasing under-prediction can also be seen. The legend description can be found in the caption of Fig. 5.12.	48
5.15	The upper two plots show the closure test for the not reconstructed muon on the left and for electrons on the right for $t\bar{t}$ and W^\pm +jets combined. On the bottom the same is shown for the out of acceptance background contribution. The legend description can be found in the caption of Fig. 5.12.	49
5.16	This plot shows the closure test for the $t\bar{t}$ and W^\pm +jets MC combined as a function of the number of primary vertices. The MC was reweighted according to the full 2011 pileup scenario. The legend description can be found in the caption of Fig. 5.10	52
5.17	These plots show the closure test for the number of primary vertices separated for not isolated muons (left) and not isolated electrons (right), for $t\bar{t}$ (top), and W^\pm +jets (bottom). The method shows no dependency on the number of vertices neither for $t\bar{t}$ nor for W^\pm +jets events. The legend description can be found in the caption of Fig. 5.12.	53
5.18	The two upper plots show the closure test for the not reconstructed electrons (right) and muons (left) for $t\bar{t}$ as the number of vertices while the two lower plots show the same distribution but for the W^\pm +jets sample. The legend description can be found in the caption of Fig. 5.12.	54
5.19	This plot shows the relative difference between Data-driven Prediction on MC and MC Expectation (dots with error band). Also a fit with a constant is shown(red). The blue lines show the ± 1 sigma envelope of a linear fit relative to the constant fit.	57
6.1	This sketch illustrates the Rebalance and Smear method used to estimate the QCD background contribution [2].	60
6.2	This sketch illustrates the γ +jets method used for the $Z \rightarrow \nu\nu$ background estimation.	61
6.3	This figure shows a typical hadronic τ response template used for the background estimation [2].	62

6.4	H_T (left) and \cancel{H}_T (right) distributions in data compared to the combined data-driven background predictions and to the SUSY LM5 benchmark scenario. The ratio of the selection on data to the combined data-driven background predictions can be found on the bottom. The hatched area represents the combined systematic and statistical uncertainties on the prediction [2].	63
6.5	Summary of backgrounds estimated from data and observed events in data for 14 search regions used in the analysis and presented in Tab. 6.1 [2] . . .	63
6.6	Both plots shows the interpretation of the results within the cMSSM model for the $m_0, m_{1/2}$ plane on top and the same limits translated to the $m_{\tilde{g}}, m_{\tilde{q}}$ plane on bottom. Everything below the observed limit (black line) is excluded at 95% CL. The dashed line with the yellow band shows the expected limit together with the ± 1 sigma uncertainty band.	66
6.7	Feynman diagram of simplified models. Left: gluino pair production; right: squark pair production.	67
6.8	(Top) Observed and (Bottom) Expected 95% C.L. exclusion limits for the (a) gluino pair production (topology T1), and (b) squark pair production (topology T2).	68
8.1	This plots show the closure tests for W^\pm +jets separated for the not isolated (top), not reconstructed and out of acceptance fraction for muons (left) and electrons (right). Good agreement for the shape can be observed. The legend description can be found in the caption of Fig. 5.12.	70
8.2	These plots show the closure tests for the out of acceptance electrons (top) and muons (bottom) for $t\bar{t}$, as the number of vertices. The legend description can be found in the caption of Fig. 5.12.	71

1 Introduction

The Standard Model (SM) of particle physics is one of the most successful scientific theories. It has been extraordinary successful, not only in describing observed interactions and the production of particles, but also predicting new particles.

Build on gauge groups, the SM has shown its predictive power to a high precision, especially in electroweak processes, which have been tested at LEP to a very high accuracy. The prediction and later discovery of the W^\pm , Z boson, which mediate the weak force, and of the b and t quarks has further increased the credency in the Standard Model. Despite all successes, experimental and theoretical arguments suggest that the Standard Model can only be consider a low energy approximation of a more fundamental theory.

For example Supersymmetry is able to solve many problems of the Standard Model in an elegant and convenient way. One prediction of Supersymmetric models is the existence of new massive particles. Interpretation of experimental results and phenomenological arguments suggest particle masses around the TeV scale, placing them in reach of the Large Hadron Colliders (LHC).

One of the main goals of the LHC and its two main experiments ATLAS and CMS is the search for these non SM particles. This thesis describes a search for such particles in events with jets and missing transverse momentum at CMS. Evidently it is crucial to predict the rate of such events due to Standard Model processes such as the production and decay of W^\pm bosons. The main focus of this thesis therefore is on one of the background estimation methods used to predict SM events involving not identified electrons and muons originating from W^\pm decays leading to such a signature. The sum of the SM background estimations contributing to this analysis, is compared to observed events in the luminosity of 4.98 fb^{-1} collected by CMS in 2011. No excess over the Standard Model expectation has been found. The obtained exclusion limits are among the most sensitive limits on SUSY up to date.

This thesis starts with a short introduction to the Standard Model and Supersymmetry (Sec. 2) followed by a description of the LHC and the CMS detector and its components (Sec. 3). Next the concept of jets with missing transverse momentum analysis is introduced (Sec. 4) followed by a detailed discussion of the lost-lepton method (Sec. 5). The last part describes the other contributing background estimations, closing with the interpretation of the results within the cMSSM and Simplified Models (Sec. 6).

2 Theory

2.1 Standard Model

During the 20th century the Standard Model of particle physics (SM) has been developed. The SM is a quantum field theory based on gauge invariance including all fundamental particles, leptons and quarks, and three fundamental forces, Quantum Chromodynamics (QCD)(Sec. 2.1.4) and Quantum Electrodynamics (QED)(Sec. 2.1.2) unified with the weak force to the electro-weak force (Sec. 2.1.3). In addition the Higgs mechanism (Sec. 2.1.5) is introduced in order to generate masses for the weak gauge bosons and all fermions. Except for the Higgs-boson all particles and forces have been found experimentally. However, new LHC and Tevatron results have found consistently candidate events for a Higgs-boson with a mass of about 126 GeV [3] [4] [5].

This section covers a short introduction to gauge theory and the Dirac equation followed by the derivation of Quantum Electrodynamics (QED) from gauge theory and a phenomenological description of the strong force (QCD), the weak force and its unification with QED. Also the concept of the Higgs mechanism is briefly described. The last part covers some of the unresolved problems within the SM suggesting a more fundamental theory.

2.1.1 The Dirac equation and gauge groups

This section discusses the Dirac equation followed by an overview of the gauge groups, which introduce the three fundamental interactions.

By combining quantum mechanics and special relativity the relativistic energy momentum relationship ($m^2 = E^2 - p^2$) had to be modified in analogy to the Schroedinger equation by replacing the energy E and the momentum p by the quantum mechanical operators $\hat{p} = -i\nabla$ and $\hat{E} = i\frac{\partial}{\partial t}$.

The resulting Dirac equation describes all fundamental fermions with spin 1/2 by four component spinor fields $\Psi(\bar{\Psi})$ ¹:

$$\mathcal{L}_{Dirac} = \bar{\Psi}i\gamma^\mu\partial_\mu\Psi - m\bar{\Psi}\Psi.$$

These four components introduce two solutions with negative energy. These solutions can be interpreted as particles moving back in time called anti-particles. These anti-particles carry the same but opposite charge.

Fig. 2.1 shows all fermions and gauge bosons included in the SM. The fundamental fermions can be divided into two species, leptons and quarks.

The charges of a particle determine via which force it interacts. All fermions except neu-

¹The adjoint spinor $\bar{\Psi} = \Psi^\dagger\gamma^0$ with Ψ^\dagger being the conjugated transpose of Ψ and γ^0 one gamma matrices [6].

trinos are weakly and electrically charged. Quarks inherit also a color charge. Neutrinos only interact weakly thus carrying only a weak charge.

Three Generations of Matter (Fermions)				
	I	II	III	
mass→	2.4 MeV	1.27 GeV	171.2 GeV	0
charge→	$\frac{2}{3}$	$\frac{2}{3}$	$\frac{2}{3}$	0
spin→	$\frac{1}{2}$	$\frac{1}{2}$	$\frac{1}{2}$	1
name→	u up	c charm	t top	Y photon
Quarks	4.8 MeV $-\frac{1}{3}$ $\frac{1}{2}$ d down	104 MeV $-\frac{1}{3}$ $\frac{1}{2}$ s strange	4.2 GeV $-\frac{1}{3}$ $\frac{1}{2}$ b bottom	0 0 1 g gluon
	<2.2 eV 0 $\frac{1}{2}$ ν_e electron neutrino	<0.17 MeV 0 $\frac{1}{2}$ ν_μ muon neutrino	<15.5 MeV 0 $\frac{1}{2}$ ν_τ tau neutrino	91.2 GeV 0 1 Z ⁰ weak force
	0.511 MeV -1 $\frac{1}{2}$ e electron	105.7 MeV -1 $\frac{1}{2}$ μ muon	1.777 GeV -1 $\frac{1}{2}$ τ tau	80.4 GeV ± 1 1 W [±] weak force
Leptons				Bosons (Forces)

Figure 2.1: This figure contains fermions and gauge bosons of the SM. The Higgs boson is not included since its existence has still not been verified by experiments.

The three forces are introduced by gauge symmetry groups ($SU(n)$):

1. $U(1)_Y$: Phase rotation introducing the electromagnetic forces (Sec. 2.1.2).
2. $SU(2)_L$: Weak isospin rotation explaining the weak force, combined with the $U(1)_Y$ to the electroweak force (Sec. 2.1.3).
3. $SU(3)_C$: Rotation of the color charge leading to the strong force (Sec. 2.1.4).

To keep this thesis concise while including all necessary theoretical explanations gauge invariance is only discussed in detail for QED. The weak, electro-weak unification and the strong force is only described phenomenologically.

2.1.2 Quantum Electrodynamics (QED)

This section demonstrates how invariance under a $U(n)$ symmetry group leads to the introduction of forces. This is being discussed for $U(1)$ with the electric charge q as generator leading to electromagnetic interactions.

The basic idea of invariance is described by the Noether Theorem [6] stating that invariance under a global $U(1)$ phase transition $\Psi \rightarrow \Psi e^{-i\alpha}$ leads to the conservation of a charge q and the corresponding current $J^\mu = q\bar{\Psi}\gamma^\mu\Psi$. The Dirac equation is invariant under such a global phase transition:

$$\mathcal{L}_{Dirac}(\Psi \rightarrow \Psi e^{-i\alpha}, \bar{\Psi} \rightarrow \bar{\Psi} e^{+i\alpha}) = \mathcal{L}_{Dirac}(\Psi, \bar{\Psi})$$

This also implies that the current and thus the electric charge is conserved.

The interaction of particles via the electromagnetic force can be introduced by requiring invariance of the Lagrangian under local gauge transformations $U(1)$ depending on the space-time x :

$$\Psi \rightarrow \Psi e^{-i\alpha(x)}.$$

With the usual space time derivatives ∂_μ this is not possible. To restore local invariance the space time derivative has to be modified by including a new gauge field A_μ with the following transformation:

$$A'_\mu = A_\mu - \frac{1}{e}\partial_\mu\alpha(x).$$

The partial derivate is substituted by the covariant derivative D_μ defined as

$$D_\mu = \partial_\mu - ieA_\mu$$

resulting in the local gauge invariant Lagrangian:

$$\mathcal{L} = \bar{\Psi}i\gamma^\mu\partial_\mu\Psi - m\bar{\Psi}\Psi + e\bar{\Psi}i\gamma^\mu\Psi A_\mu$$

The additional term describes the interaction of the photon A_μ with the fermion. An additional term $F_{\mu\nu} = \partial_\mu A_\nu - \partial_\nu A_\mu$ ² has to be added to include the energy stored in the electromagnetic field:

$$\mathcal{L} = \bar{\Psi}i\gamma^\mu\partial_\mu\Psi - m\bar{\Psi}\Psi + e\bar{\Psi}i\gamma^\mu\Psi A_\mu - \frac{1}{4}F^{\mu\nu}F_{\mu\nu}.$$

This is the full QED Lagrangian including the kinetic energy of the particle and its mass together with the interaction of the particle with the Photon and the energy stored in the electromagnetic field. Similar calculations for $SU(2)_L$ and $SU(3)_C$ lead to weak and strong interactions.

2.1.3 The weak force and the electroweak unification

The weak force can be introduced by the $SU(2)_L$ group with the three Pauli matrices as generators. The Z and the W^\pm bosons are introduced as gauge bosons. In contrast to the other gauge bosons the Z and W^\pm bosons have a mass of $M_W = 80.4$ GeV and $M_Z = 91.2$ GeV. The resulting mass terms are not gauge invariant. Instead of direct mass terms the Z and W^\pm couple to the Higgs field (Sec. 2.1.5), which introduces gauge invariant indirect mass terms.

²This is the antisymmetric field strength tensor known from classical electrodynamics.

The weak force has been found to be maximally parity³ violating leading to exclusive left-handed⁴ weak interactions for particles and right handed interactions for anti-particles. The masses of the vector bosons suppresses interactions above the natural range of 10^{-18}m , determined by the Heisenberg uncertainty principle, making the weak force appear to be weak at energies below 100 GeV.

The electroweak unification describes the weak and the electromagnetic force as two aspects of the same force. The combination can be achieved with a $SU(2)_L \times U(1)_Y$ group. The obtained covariant derivative D^μ includes 4 generators B^μ and W_i^μ with $i = 1, 2, 3$.

$$D^\mu = \partial^\mu + \frac{i}{2}g\vec{\tau}_i \cdot \vec{W}_i^\mu + i\frac{g'}{2}YB^\mu \quad (2.1)$$

with g, g' being coupling constants, τ_i defined to be the Pauli matrices. The W^\pm are now mixtures of the $W_{1,2}$ fields:

$$W^\pm = \frac{W_1 \pm iW_2}{\sqrt{2}}.$$

The A^ν and Z^ν are orthogonal linear combinations of the W_3 and B fields related via the Weinberg angle $\vartheta_W = 28^\circ$ which had to be measured by experiments [7].

$$A^\mu = B^\mu \cos\vartheta_W + W_3^\mu \sin\vartheta_W$$

$$Z^\mu = -B^\mu \sin\vartheta_W + W_3^\mu \cos\vartheta_W$$

The fields $W_{1,2}$ mix to form the charged current. The electromagnetic force now couples via the hypercharge Y (instead of the plain electric charge (q)): To account for the exclusive coupling of the weak force to left handed particles $\vec{T} = \frac{1}{2}\vec{\tau}$ is defined for left handed and $\vec{T} = 0$ for right handed particles. The electromagnetic force still couples to both handed particles because $Y \neq 0$.

2.1.4 QCD

The third force which is included in the SM is the strong force with the associated color charge and gluons as gauge bosons. The only particles carrying color charges are quarks⁵ and gluons. Experiments have shown that the color charge comes in three options introducing a new degree of freedom⁶.

The gauge structure of this force is the $SU(3)_C$ group which is similar to the $U(1)$ group. The more complex structure of the $SU(3)_C$ leads to eight color charged gauge bosons⁷ and to three and four vertex gluon-gluon interactions. The charged gauge bosons lead to the consequence that the strong force increases over distance resulting in the exclusive existence of color neutral bound states of quarks⁸ called hadrons. Two different kind of

³Parity being invariance of physics under space inversion eg. $\vec{x} \rightarrow -\vec{x}$

⁴The projection of the spin vector on the momentum vector has a positive sign.

⁵Anti quarks carry an anti-color.

⁶For example the ratio of $e_+e_- \rightarrow \frac{\text{hadrons}}{\mu_+\mu_-}$ being three times larger than expected suggesting a new degree of freedom.

⁷Either one color or anti color.

⁸A bound state is considered color neutral when it either consists of one color and its anti color or includes all three colors.

hadrons have been observed. Baryons, consisting of three quarks, each carrying a different color and mesons which consist of a quark and an anti-quark carrying the same color and anti-color respectively.

For example the proton consists of quarks and gluons called partons which have to be measured by experiments like HERA [8].

The residual of the strong force is responsible for keeping the nucleons together.

2.1.5 The Higgs Mechanism

The symmetry of the $SU_Y(1) \times SU_L(2)$ has to be broken to give masses to the weak vector bosons while preserving gauge invariance. Also the photon and the gluons have to remain massless.

Peter Higgs [9] among others introduced a rather simple solution to this problem.

His idea was to introduce a new underlying field called Higgs field which is present everywhere in space with a degenerated⁹ lowest energy state (vacuum expectation value). The corresponding Lagrangian remains gauge invariant. The W^\pm and Z gauge boson can now couple to this field resulting in mass gathering proportional to the strength of the coupling. This symmetry breaking can be achieved while leaving the $U(1)_Y \times SU(2)_L$ symmetry unbroken therefore gauge invariant and leaving the photon massless. The $SU(3)_C$ is also not influenced.

The simplest way to produce such a so called "spontaneous" symmetry breaking is a complex scalar $SU(2)$ doublet with a non zero vacuum expectation value:

$$\Phi(x) = \begin{pmatrix} \Phi_a(x) \\ \Phi_b(x) \end{pmatrix} \quad (2.2)$$

This potential can also be expressed in its four independent fields η_i and a constant v :

$$\Phi(x) = \frac{1}{\sqrt{2}} \begin{pmatrix} \eta_1(x) + i\eta_2(x) \\ v + \eta_3(x) + i\eta_4(x) \end{pmatrix} \quad (2.3)$$

With a gauge transformation $\eta_{1,2,4}$ can be absorbed by the boson fields W^\pm and Z resulting in indirect mass terms. The remaining potential

$$\Phi(x) = \frac{1}{\sqrt{2}} \begin{pmatrix} 0 \\ v + \eta_3(x) \end{pmatrix} \quad (2.4)$$

is now independent of $\eta_{1,2,4}$. The corresponding gauge invariant Lagrangian is:

$$\mathcal{L}_\Phi(x) = (D^\mu \phi(x))(D_\mu \phi(x)) - \mu^2 |\phi(x)|^2 - \lambda |\phi(x)|^4 - \frac{1}{4} F^{\mu\nu}(x) F_{\mu\nu}(x) \quad (2.5)$$

with $\phi(x)$ being the scalar Higgs field, $F^{\mu\nu}(x)$ the Lagrangian density of the free field, D^μ the covariant derivative, μ^2 and λ being real parameters. No mass-term for the γ is being introduced therefore the γ remains massless. A minimum of the potential exists at

$$\nu = \sqrt{\frac{-\mu^2}{\lambda}}$$

⁹i.e. no longer invariant under symmetry transformation

when $-\mu^2 > 0$ and if λ is a real parameter. This minimum can be identified with the vacuum expectation value of the Higgs field, also included in Eq. 2.4. A massive spin 0 Higgs boson with the mass of $M_H = \sqrt{-2\mu^2}$ is the consequence of the remaining free Higgs field $\eta_3(x)$.

In addition to the mass generation of the weak vector bosons the Higgs mechanism provides also an elegant way for fermions to acquire masses¹⁰.

2.2 Open questions and problems of the SM

Despite all achievements of the SM in not only describing but predicting particles and interactions it can only be seen as a low energy approximation of a more fundamental theory. The following list provides some short comings of the SM and experimental results hinting towards new physics for which a popular approach will be discussed in the following chapter.

- The weak and electromagnetic force have been unified suggesting the idea of unifying every force within a theory of everything. Such Grand Unified Theories (GUTs), unify the electro-weak and the strong force at an energy around 10^{15} GeV in a gauge group G with one single coupling. The SM can not provide such a unification at such a scale.
- All the particles masses can not be predicted within the SM but have to be measured. Further the exact same value of the electric charge for the electron and the proton can not be explained. Also at very high energies radiative corrections to certain processes diverge leading to unitarity violation.
- Astrophysical observations have shown discrepancies between expected mass distributions calculated from galaxy gravitational lensing and the visible amount of matter, suggesting a huge amount of dark matter, about 23% of all energy within the universe [10]. Dark matter does not interact electromagnetically or strongly making it invisible to direct observations. The neutrinos are the only candidates within the SM for such matter but observations require dark matter to be a lot heavier than the upper limit on the neutrino masses.
- Another problem within the SM is the so called "Naturalness". The bare Higgs mass M_H introduced in Sec. 2.1.5 has to be corrected by higher order quadratic loop corrections. If the SM is valid up to the Plank scale (10^{19} GeV), at which gravity becomes as strong as the other forces, loop corrections would increase the Higgs mass significantly. To reduce the mass of the Higgs boson to the favored $O(100 \text{ GeV})$ regime, so called "fine tuning" is needed. Different independent loop corrections with opposite sign would have to cancel each other to a precision of 10^{-31} which is not convincing.
- A different approach to solve the Naturalness problem is the introduction of a cut-off energy scale at which new physics is expected. A cut-off at the TeV scale solves the Naturalness problem by demanding new particles with such a mass. Supersymmetry

¹⁰In principle neutrinos could also gather masses in the same way but the SM assumes them to be massless.

as discussed in Sec. 2.3 can provide such particles and therefore is believed to be realized at the TeV scale making it potentially discoverable by LHC experiments.

- Furthermore every attempt to combine gravity and the SM has failed so far.
- Also the observed asymmetry of matter and anti-matter can not be explained.

These reasons among others lead to the assumption that the SM can only be seen as a low energy approximation of a more fundamental theory.

2.3 Supersymmetry

Many theories are available which solve some of these shortcomings. A very elegant approach of solving the fine tuning problem and providing a dark matter candidate is Supersymmetry (SUSY). Since this thesis focuses on the search for new physics and especially for SUSY particles an introduction to SUSY will be presented in the next section. Supersymmetry (SUSY) is the last possible symmetry operation which can be incorporated into the Poincaré group [11]. The SUSY generator Q relates fermions and bosons and in its simplest version introduces for each SM particle a supersymmetric partner with a shift in spin of $1/2$. Therefore, the SUSY partners of the fermions are bosons with spin 0 called sfermions and the partners of the SM gauge bosons are spin $1/2$ fermions called gauginos. In addition another Higgs doublet has to be introduced resulting in five Higgs bosons instead of the one predicted by the SM. The color neutral gauginos and the higgsinos mix to form four charged charginos $\chi_{1,2}^{\pm}$ and four neutral neutralinos χ_{1-4}^0 . The generator Q commutes with all SM generators resulting in identical quantum numbers and masses of the related particles.

Besides the argument that it can in principle be added to the Poincaré group SUSY can also solve many problems of the SM for example the "Naturalness" problem. The quadratic loop corrections from SM particles are countered by the SUSY particles that enter with opposite sign.

SUSY allows terms which violate baryon- and lepton-number conservation. One consequence is that the proton becomes unstable. The decay is mediated by the product of one lepton- and one baryon-number violating term. The lower limit on the life time of the proton has been found to be $6.6 \cdot 10^{33}$ years [12] [13] putting tight boundaries on the decay and therefore on the corresponding terms in the Lagrangian.

To recover the proton stability a new conserved quantity, R -parity, is introduced:

$$R = (-1)^{3(B-L)+2S}$$

with B being the baryon-number, L the lepton-number and S the spin. SM particles have $R = 1$ and SUSY particles have $R = -1$ prohibiting the mixing between SM and SUSY particles.

An interesting consequence of R -parity conservation is the stability of the lightest supersymmetric particle (LSP) making it a natural candidate for Dark Matter if it interacts only weakly.

So far extensive searches have been conducted for SUSY but none has found any direct evidence for its existence yet (eg. [14] [15] [16]). The SUSY particles have to have the

same mass as the SM partners but no such particles have been found. This problem can be solved when SUSY is a broken symmetry. For soft broken SUSY more than 100 new free parameters have to be introduced in the most general case.

The breaking mechanism is believed to take place at the GUT scale in a so called "hidden sector" which is decoupled from the observable universe below the breaking scale. The mass term breaking is mediated via messenger interaction mediated to the observable universe. All soft breaking mechanisms involve gravity as messenger interaction. For mSUGRA gravity is assumed to be the only one.

2.3.1 SUSY breaking in the Model of Minimal Supergravity and the cMSSM

Minimal Supergravity Models (mSUGRA) are favored for presenting experimental results since they include only five free parameters which makes result interpretation easier.

In mSUGRA the mass breaking from the hidden sector is transmitted via gravity¹¹. The large amount of over 100 free parameters is reduced to only five by implying that the strength of all gauge coupling parameters become equally strong and unification of the common scalar and gaugino mass breaking terms at the GUT scale¹². The remaining free parameters are:

$$m_0, m_{1/2}, A_0, \tan\beta, \text{sign}(\mu) \quad (2.6)$$

With m_0 being the common mass breaking parameter for all sleptons, squarks at the GUT scale, $m_{1/2}$ being the mass of the gauginos at the GUT scale, A_0 is the trilinear scalar coupling between the Higgs and two sfermions, μ being the Higgs mass parameter and $\tan\beta = \frac{v_u}{v_d}$ is the ratio of the two vacuum expectation values arising from the two Higgs fields.

From renormalization group equations the couplings and masses at low energy scales can be obtained.

In mSUGRA models the ratio $\tan\beta$ is fixed were in cMSSM it can be varied. The results of this analyses are presented within the cMSSM framework and Simplified Models (Sec. 6.2.1, 6.2.2).

¹¹The graviton couples to the energy-momentum tensor for matter from general relativity. Still the Supergravity Lagrangian has some non-renormalizable parts. Therefore this can not be seen as a proper implementation of gravity but at best as a low-energy approximation.

¹² $\Lambda \approx 10^{16}$ GeV

3 LHC and CMS detector

3.1 The Large Hadron Collider (LHC)

The Large Hadron Collider (LHC) [17] [18] [19] is the largest and most complex machine every build by man. It is a circular proton-proton collider in a tunnel 100 meters below surface at the CERN research center close to Geneva, inheriting the former Large Electron Positron collider (LEP) tunnel with a circumference of 26.7 km. Fig. 3.1 shows the layout of the LHC and the vaults containing the experiments.

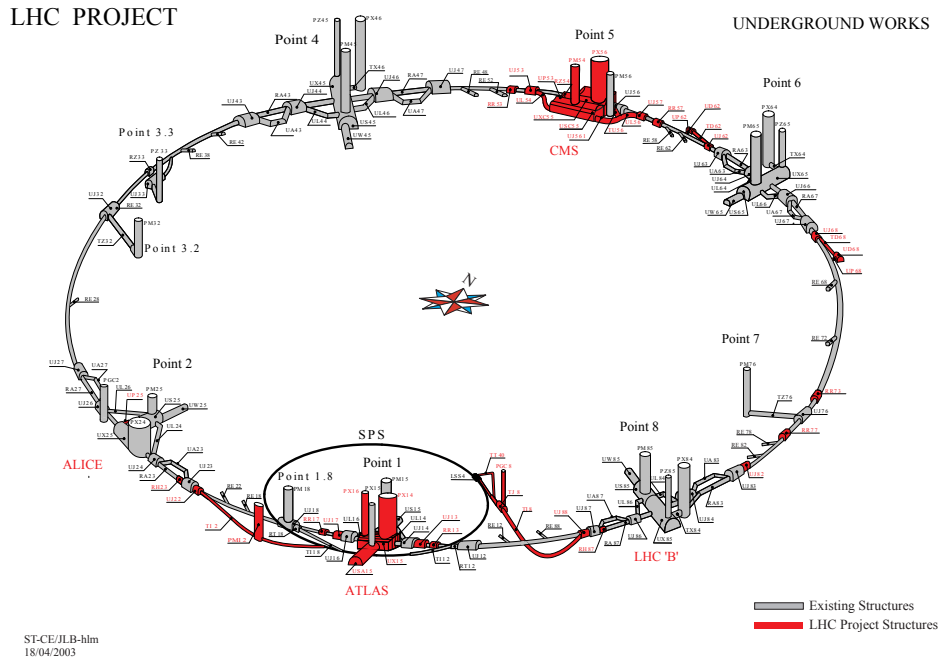


Figure 3.1: An exploded view of the CMS detector.

The LHC was designed for a center-of-mass energy of 14 TeV and a luminosity of $L = 10^{34} \text{ cm}^{-2} \text{ s}^{-1}$. The luminosity L is defined as:

$$L = \frac{N_b^2 n_b f_{rev} \gamma}{4\pi \epsilon_n \beta^*} F \quad (3.1)$$

where N_b is the number of particles per bunch, n_b the number of bunches per beam, f_{rev} the revolution frequency, γ is the Lorentz factor, F a reduction factor arising from the angel of the two beams at the interaction, ϵ_n a quantity of the parallelism of the beam

and β^* is related to the width of the beam at the interaction point.

The design Luminosity can be achieved with 2808 bunches colliding every 25 ns, an $\epsilon_n = 3.75 \mu\text{m}$ and a $\beta^* = 0.55 \text{ m}$.

Strong magnetic fields of up to 8,4 Tesla are needed to keep the high energetic protons with a maximum energy of 7 TeV circling. To achieve such high magnetic fields superconducting magnets have been chosen.

The particles are collided at specific interaction points at the four main detectors ATLAS [20], CMS [21], LHCb [22] and ALICE [23]. ATLAS and CMS are multipurpose detector designed with the focus on the discovery of the Higgs boson, search for physics beyond the SM and top physics, while LHCb focuses on the CP-violation in b-physics and ALICEs was designed to investigate quark-gluon plasma produced in heavy ion collisions.

This thesis analysis makes use of a total luminosity of 4.98 fb^{-1} [24] of proton-proton collisions with at a center-of-mass energy of 7 TeV and a peak luminosity of $L = 3.55 \cdot 10^{33} \text{ cm}^{-2} \text{ s}^{-1}$ recorded by the CMS detector during the year 2011.

The following chapter contains a description of the CMS detector and its components followed by an introduction to the physics objects and definitions relevant for this analyses and the particle flow algorithm used for particle reconstruction.

3.2 The Compact Muon Solenoid detector

One main aspect relevant for the design of the Compact Muon Solenoid (CMS) was the inclusion of the calorimeters within a strong magnetic field to measure charged particles and especially muon momenta to a high precision. To achieve high the magnetic field, a superconducting magnet was installed.

The CMS detector is built in cylindrical shape around the beam pipe with a length of 21.6 m and a diameter of 14.6 m with a total weight of of 12 500 tons. Fig. 3.2 shows an overview of the CMS detector.

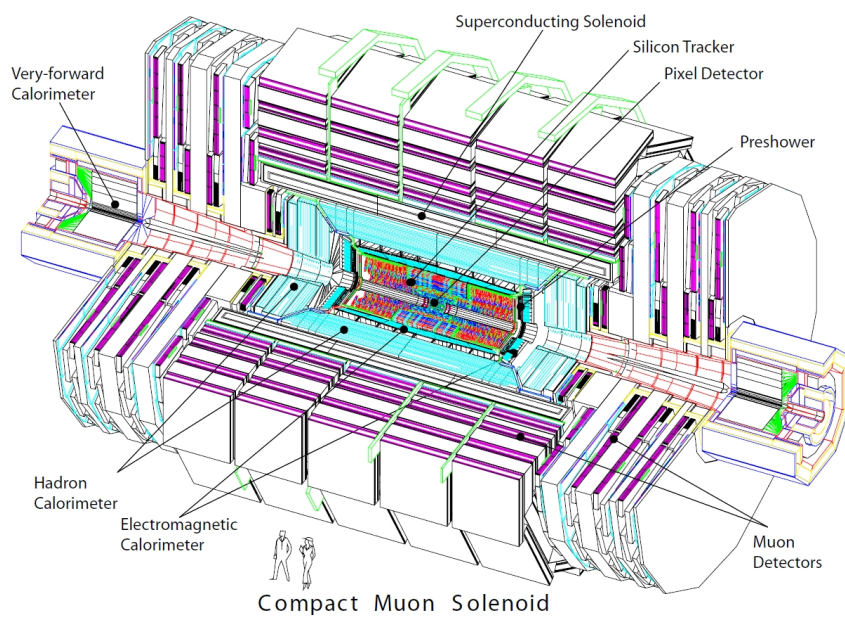


Figure 3.2: An exploded view of the CMS detector.

A right-handed coordinate system together with cylinder coordinates has been chosen by the CMS collaboration. With the z-axis pointing in the beam direction, y-axis pointing up and the x-axis pointing to the center of the LHC. The polar angel Θ is measured from the z-axis and the azimuthal angel ϕ is measured relative to the x-axis in the x-y plane. The pseudorapidity η , commonly used in high energy physics, is given by:

$$\eta = -\ln \tan \left(\frac{\Theta}{2} \right)$$

The Lorentz-invariant distance between two relativistic objects is defined as:

$$\Delta R = \sqrt{(\Delta\eta)^2 + (\Delta\Theta)^2}$$

Since the initial momentum in the beam direction (z) for interactions at hadron colliders like the LHC is unknown, only the transverse¹ momentum $p_T = p \cdot \sin\Theta$ and the transverse energy $E_T = E \cdot \sin\Theta$ is used to measure the energy and momentum of produced particles. The following layers are cylindrically build around the beam pipe:

- A silicon-based tracker (Sec. 3.2.1) at the heart of the detector designed to measure the trajectory of particles with a high precision.
- The next layer consists of the electromagnetic calorimeter (ECAL)(Sec. 3.2.2) based on scintillating crystals mainly used to detect electrons and photons.
- A preshower system has been installed in front of the ECAL endcaps, designed to identify π^0 particles.
- The Hadronic calorimeter (HCAL)(Sec. 3.2.3) surrounding the electromagnetic calorimeter is designed to measure jet energies.
- To improve the HCAL ability to measure high energetic jets a "tail-catcher" in the barrel region has also been installed.
- The outermost part of the detector consists of the iron yokes for the magnetic field together with the drift chambers together forming the muon detection system (Sec. 3.2.4).

These sub parts of the CMS detector will be discussed in greater detail in the following.

¹relative to the beam axis

3.2.1 The tracker

Fig. 3.3 shows the layout of the CMS tracker [25] [21] [26] which extends to 1.1 m in transverse direction and is approximately 5.4 m long.

The inner tracker is divided in two parts:

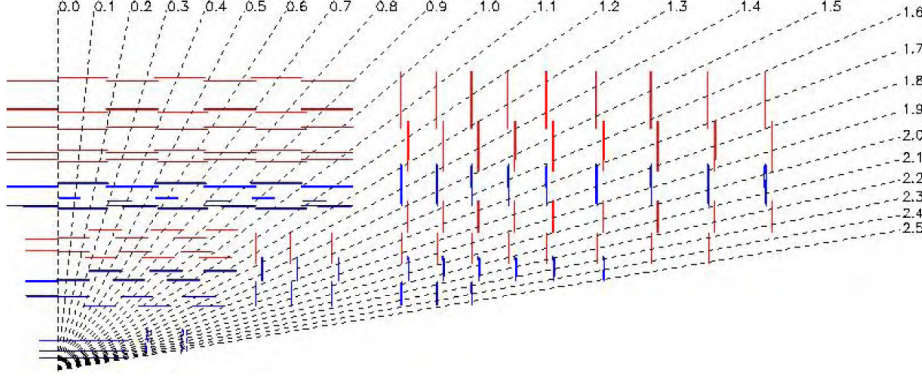


Figure 3.3: An exploded view of the CMS detector.

The pixel detector consists of 55 million pixels because close to the interaction point a high granularity is necessary due of the high particle flux. Also a high resolution of the vertex reconstruction of $25 \mu\text{m}$ and $20 \mu\text{m}$ in X and Y is needed [27]. This high resolution is especially important in measurements of b-jets since they have a relative long lifetime resulting in a measurable transverse distance of a second vertex of the decaying b-jet. The high design instantaneous luminosity leads to additional interactions in one bunch-crossing called pileup interactions. These usually soft interactions need to be separated from the hard process which requires good resolution.

The second part is the silicon strip detector located outside of the pixel detector. A total area of 200 m^2 is covered by 9.6 million strips covering, the region up to $|\eta| \approx 2.4$.

The reconstruction efficiency of muons with a $p_T > 1 \text{ GeV}$ is about 99%. Combined with the strong magnetic field tracks of charged particles can be measured to reconstruct the transverse momentum according to this equation:

$$p_T = 0.3 \frac{\text{GeV}}{e \cdot \text{T} \cdot m} \cdot B \cdot \rho$$

with B being the magnetic flux density, ρ the tracks radius of curvature in the transverse plane, m and e being the mass and the electric-charge of the particle.

3.2.2 The Electromagnetic Calorimeter

The homogeneous electromagnetic calorimeter (ECAL) [25] [21] [28] was build around the inner tracker system consisting of lead-tungstate crystals, which have a radiation length² $X_0 = 0.98 \text{ cm}$ and a Moliere radius of $R_M = 2.2 \text{ cm}$ resulting in a compact size which is especially important to fit the tracker, ECAL and the HCAL inside of the Superconducting

²The length after which an electrons energy has decreased to $\frac{1}{e}$ of its original energy.

Solenoid.

The barrel part of the ECAL consists of 61 200 crystals covering $|\eta| < 1.479$ whereas the two endcaps are build up of 14 648 crystals covering $1.479 < |\eta| < 3.0$.

The crystals are robust against radiation and emit 80% of the light radiated within the 25 ns between two bunch crossings at design LHC operation. The ECAL has an energy resolution of

$$\left(\frac{\sigma}{E}\right)^2 = \left(\frac{S}{\sqrt{E}}\right)^2 + \left(\frac{N}{E}\right)^2 + C^2$$

with $S=3\%$ as stochastic term, $N = 124 \text{ MeV}$ as noise term and $C = 0.26\%$ as constant term. The response of a calorimeter is defined to be the measured energy divided by the true energy of a particle showering. Hadrons and electrons have a different response with the ratio given by $\frac{e}{h} \approx 1.6$. Noise is being suppressed by only reading out cells with an energy deposited above a certain threshold.

Good performance of the ECAL has been observed however some of the about 70 000 crystals have a dysfunctional readout.

3.2.3 The Hadronic Calorimeter

The Hadronic Calorimeter (HCAL) [25] [21] [29] consists of alternating layers of brass as absorber and plastic scintillators. To support these heavy structures the innermost and outermost layers are made of steel. The ECAL and HCAL are arranged in towers read out by single wavelength shifting fibers.

The HCAL consists of four parts:

- The hadron barrel (HB) covering the central part of the HCAL with $|\eta| < 1.4$ made of 2304 towers with a segmentation of $\Delta\eta \times \Delta\Phi = 0.087 \times 0.087$. The absorbers have the thickness of 5.05 cm for each of the inner eight layers and 5.56 for the outer six layers. The scintillators located in between the absorber layers are 3.7 mm thick except for the very first layer behind the ECAL which is 9 mm thick.
- Due to the limited space available by keeping the HCAL inside the Solenoid, jets may not deposit their entire energy within this part. Scintillators are also outside the coil with an interaction length of $1.4/\sin(\Theta)$ called the hadron outer detector (HO)³.
- The hadron endcaps (HE) make up the third part. Here only 87 mm thick brass and one 3.7 mm thick scintillator was used.
- The last part the hadron forward (HF) is located close to the beam axis at $3.0 < |\eta| < 5.0$. This part is made of steel absorber and radiation hard quartz fibers. It is constructed out of 18 wedges located 11 m from the interaction point thus increasing the coverage helping to measure missing transverse momentum.

Like the ECAL the HCAL is a non-compensating calorimeter with $\frac{e}{h} \approx 1.4$. A read out threshold is also used to reduce noise (called zero suppression).

³This part was not used for the analyzed data in this thesis since the noise level was not sufficiently small.

3.2.4 The Solenoid and the Muon Chambers

The superconducting solenoid with a length of 12.9 m, a thickness of 1.8 m and an inner diameter of 5.9 m is one of key element of the CMS detector dominating its design. 19.5 kA of current are used to provide the 3.8 Tesla magnetic field which permeates the calorimeter and tracker.

The muon chambers [25] [21] [30] located outside the magnetic coil partially taking advantage of the material used for the solenoid consist of four muon stations covering $|\eta| < 2.4$. The muon barrel region (MB) uses aluminum drift tube chambers (DT) to achieve high resolution for muons. The endcaps (ME) consist of cathode strip chambers (CSCs). In this forward direction a higher rate of muons is expected explaining the use of CSCs due to their fast response. The coverage is being completed by resistive plate chambers (RPCs) included in both parts of the muon chambers. These RPCs have a much lower momentum resolution than the other parts of the muon chambers but the very fast response time and the excellent time resolution is needed to identify the correct bunch crossing. These muon detectors are arranged in four stations in both detector regions.

Together with the inner tracker the muon system is able to achieve a muon p_T resolution between 1% and 10% up to a muon p_T of 1 TeV.

3.2.5 Trigger

At design luminosity the LHC has a bunch crossing rate of 40 MHz. At this rate the event size of approximately 1 MB per event leads to a too high output of data to be stored and processed. Since not all events include interesting physics a trigger system [31] [32] only collecting events fulfilling predefined criteria is installed.

The trigger is organized in two stages:

- The pure hardware⁴ level 1 trigger(L1) using only detector parts which have a fast readout rate, the calorimeters and the muon chambers. These informations are combined by simplified object algorithms to loosely define electrons, photons, muons and jets. From these algorithms interesting events are selected by demanding a certain energy threshold and or leptons or jets to reduce the event rate to 100 kHz⁵. To keep the information until the L1 has decided weather an event will rejected or not the full detector output is stored in a pipeline for 3.2 μ s.
- The software based high level trigger (HLT) which is also used to reduce the amount of events further by a factor of 100 to be able to store the events at a rate of ≈ 100 MB/s. This trigger can access the full detector information enabling more advanced trigger algorithm definitions. The advantage of software based triggers compared to hardware based ones is the flexibility in the design of individual trigger paths. Restrictions from the aim of a reduction factor of 100 together with the demands from physical analysis dominate the trigger paths designs.

Each stored event inherits the L1 and HLT trigger informations.

⁴Pure hardware trigger was chosen since it has increased speed compared to software triggers.

⁵Prescaled trigger paths are used to collect only every x-th collision of one type of interaction, important for collisions which have a too high rate to record every collision.

3.3 Particle identification and physical object definitions

This section covers particle identification of the CMS detector and physics quantities used in this thesis.

The particles emerging from the interaction point at the center interact differently with the detector components enabling distinguishing between them. Fig. 3.4 illustrates typical interactions with the detector components.

This list covers typical signatures of photons, electrons, muons, taus, jets and only weakly interacting particles:

- Photons are electrical neutral particles thus leaving in most cases no track in the tracker. First interactions happens typically in the ECAL. Due to the depth of $X_0 = 25$ of the ECAL photons are most likely to deposit all energy distributed only over a few crystals in the ECAL. Approximately 50% of all photons already convert to e^-e^+ pairs within the tracker but usually the major fraction of energy is deposited in the ECAL [33].
- Electron identification is difficult because of the emission of Bremsstrahlung. Due to the high magnetic field and the strong resulting bending of the electron trajectory the emitted photons are spread across the detector. Clustering algorithms are used to take Bremsstrahlung into account. In particular Superclusters (clusters of clusters) together with a matched track from the tracker are used in the reconstruction of electrons [34].
- Muons with a $p_t > 2.5$ GeV loose only a small fraction of their energy within the detector [35] making them so so called minimize ionizing particles. They are the only particles that reach the muon chambers making the muon identification very easy.
- Taus have a too short lifetime to interact with the detector. Instead only the decay products can be observed. Their are special algorithms designed to identify taus but this thesis does not include any tau signatures.
- In the hard interaction⁶ quarks and gluons may be produced. As discussed in Sec. 2.1.4 color charged particles can only exist in bound states leading to the formation of jets which consist of many emitted hadrons close to each other. These hadrons can either be electrically neutral, leaving no track in the tracking system or electrically charged. Neutral hadrons will only interact with the HCAL whereas charged hadrons also leave a signal in the tracker and the ECAL. The main fraction of energy of both types is always deposited within the HCAL. The effect referred to as "punch through" occurs when a jet has too much energy to be stopped within the HCAL. This is the main source for high energetic jet mismeasurements.
- Weakly interacting particles will not interact with any component of the detector. They can only be measured indirectly by taking advantage of the initial state of no transverse momentum. An imbalance in the transverse momentum plane hints to the production of, such a particle.

⁶Hard interactions refer to a high energy transfer in the parton parton interaction.

These particles are all reconstructed with the particle flow algorithm discussed in Sec. 3.4. The reconstructed particles are used for the following physical quantities:

- $H_T = \sum |\vec{p}_T|$, only jets with $|\vec{p}_T| > 50$ GeV and $|\eta| < 2.5$ are considered.
- $\cancel{H}_T = -\sum(p_T)$, jets with $|\vec{p}_T| > 30$ GeV and $|\eta| < 5$ are included. A different selection than for H_T is used to avoid introducing artificial \cancel{H}_T by neglecting jets.
- $\cancel{E}_T = -\sum(p_T)$, all particles p_T found in an event.

3.4 The particle-flow algorithm

The particle-flow algorithm used by CMS is based on the idea to reconstruct all stable particles. An important ingredient is the combination of all detector component information in the particle reconstruction procedure. The first step is the definition of elementary signatures. One being the identification of charged particles from inner tracker and muon chamber informations. Another is the clustering procedure. Calorimeter information is used to define clusters from adjacent calorimeter cells with energy deposits.

Since particles can have several of these signatures they are linked to blocks in order to improve accuracy by combining signatures from different subdetector parts and to avoid double-counting of signatures. For example Bremsstrahlung photons are tried to be identify by matching tangential extrapolated clusters from the ECAL to a track in the tracker. The resolution of muons is improved by linking tracks from the inner tracker with the muon system.

The final particle reconstruction is done according to dedicated quality criteria. For each identified particle the tracks and energy deposition are removed from an event to avoid double counting.

First the muons are identified, followed by the electrons. The remaining tracks are considered to be charged hadrons tracks and are matched to clusters energies. HCAL and ECAL clusters that can not be matched to a track are interpreted as neutral hadrons. Photons are identified if only ECAL clusters remain that can not be matched to a track.

The particle-flow algorithm has improved especially the jet measurements performance [36] [37].

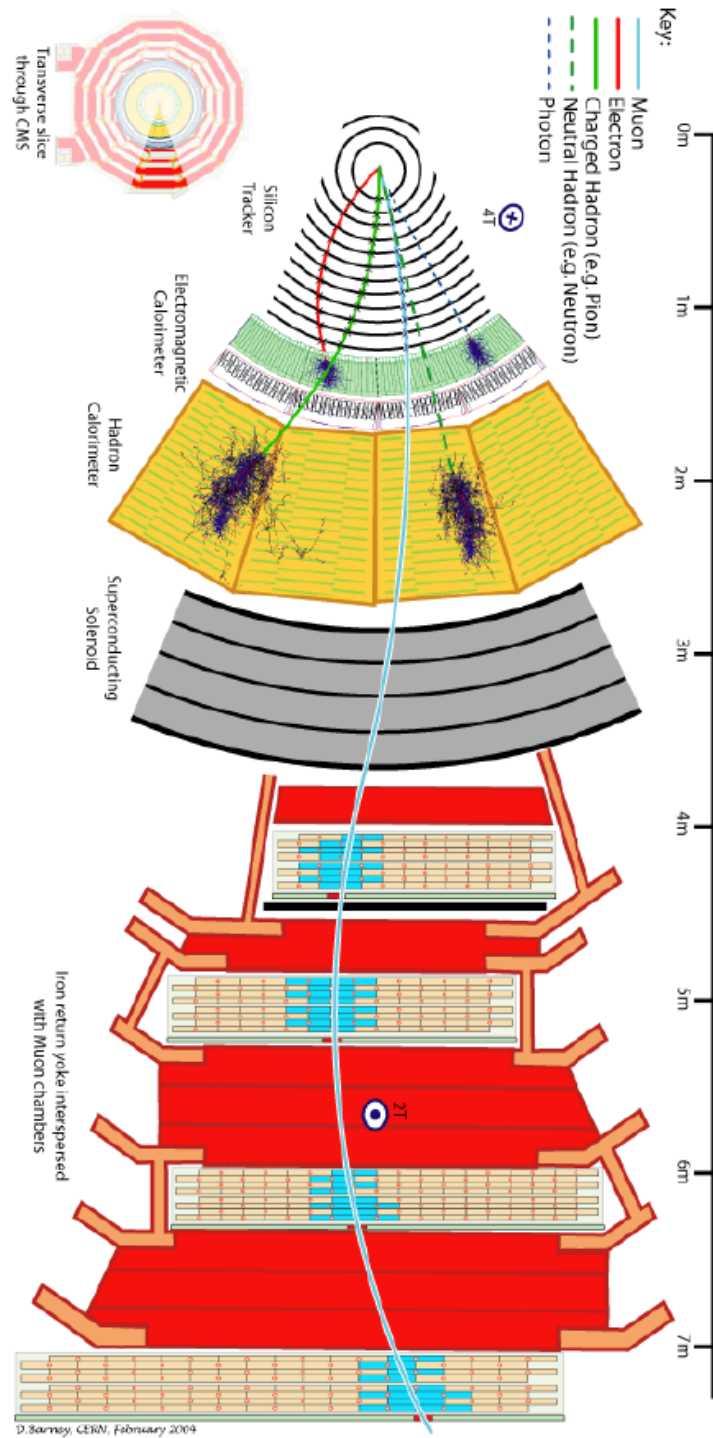


Figure 3.4: This figure shows the transverse slice through the CMS detector with typical particle interaction signatures with the detector.

4 The concept of jets with missing transverse momentum analysis

Short summary of the method:

- Select one well isolated muon
- Reconstructed transverse mass of $m_{T\bar{W}} < 100$ GeV
- Correct for inefficiency of the $m_{T\bar{W}}$ cut (parametrized in NJet about 90% eff)
- Correct for dileptonic events (over estimated correct down by 1.5% of the total control sample)
- Weight for iso, reco out of acceptance muons
- Weight for out of acceptance, reco and not isolated electrons

the uncertainties:

- statistics of the control sample up to 100%
- uncertainty on the transverse mass cut 3.2% this is something like 50% includes statistical uncertainty of the eff maps the rest on the correction factor of the cut handwaving
- acceptance pdf uncertainty and statistical uncertainty on the used eff maps
- Di-Lep correction also handwaving
- Elec, Muon iso/reco all included statistical uncertainty and uncertainty obtained by comparing tag and probe eff obtained from Z events data and MC
- Other SM processes. tried to select CS from qcd samples and di boson sample did not find any.... 3% conservative
- Non-Closure includes most points covers for residual problems of the method due to small statistics in the search regions

Many models of physics beyond the standard model predict events with missing transverse energy. A typical scenario includes particles which are heavy, some being stable and do not interact with the detector. For R-Parity conserving SUSY heavy gluinos and squarks¹, are expected to be produced at pp colliders like the LHC, since they are color charged. Many SUSY models predict them to decay rapidly in cascades to lighter SUSY

¹if they are kinematically accessible

particles resulting at the end in the lightest supersymmetric particle (LSP), which would be stable and leave the detector without any interaction causing an imbalance in the transverse momentum. The resulting signature is missing transverse momentum (\cancel{H}_T) from the LSP and jets leading to high H_T .

This signature is experimentally very challenging since SM processes can also lead to high H_T and \cancel{H}_T events. Therefore it is crucial to predict these background events as precisely as possible. The four following SM processes have been found to contribute to these signature:

- The QCD background arising from mismeasured jets leading to \cancel{H}_T ,
- the "Z invisible" background from $Z + \text{Jets}$ events where the Z decays to two neutrinos,
- the "hadronic τ " background, arising from $W^\pm + \text{jets}$ or $t\bar{t}$ events. The involved W bosons decay to a τ 's which decay further hadronically to jets.
- the "lost-lepton" background including $W^\pm + \text{jets}$ or $t\bar{t}$ events which decay to not identified muons or electrons in the final state.

These four main backgrounds are all data-driven² estimated.

4.1 Event Selection

The event selection is motivated by all the contributing backgrounds with some of the selection criteria introduced to reduce particular backgrounds. In the "baseline" selection events are selected according to the following criteria:

- At least 3 jets with $p_T > 50$ GeV and $|\eta| < 2.5$ are required.
- $H_T > 500$ GeV
- $\cancel{H}_T > 200$ GeV

In addition, further cuts have been introduced to reduce the backgrounds:

- $|\Delta\phi(J_n, \cancel{H}_T)| > 0.5$ rad, $n = 1, 2$ and $|\Delta\phi(J_3, \cancel{H}_T)| > 0.3$ rad with J being the jets in an event. This cut has been introduced to remove most of the QCD events including mismeasured jets, where the \cancel{H}_T is aligned to the next-to-leading jet. The cut on $\Delta\phi$ at 0.5 has been chosen to be equal to the jet cone size, while the looser cut at 0.3 retains signal efficiency.
- An explicit lepton veto rejects events including identified electrons or muons reducing the background arising from leptonic decaying W^\pm bosons which include naturally missing energy from the involved ν .

The lepton isolation criteria is defined to be as loose as possible in order to reduce $W^\pm + \text{jets}$ and $t\bar{t}$ background events. Most, but not all of the criteria for μ and electrons are the same.

Muons are required to have:

²Data-driven refers to using data events, not simulated events, to estimate the backgrounds.

- $p_T > 10 \text{ GeV}$ and $|\eta| < 2.4$.
- A track reconstructed from a combination of inner tracker and the muon system have to be matched to the primary vertex within $200\mu\text{m}$ transverse and 1 cm longitudinal.

For electrons the required conditions are:

- $p_T > 10 \text{ GeV}$ and $|\eta| < 2.5$ excluding the transition region $1.4442 < |\eta| < 1.566$

Electrons and muons must also fulfill this relative isolation variable:

$$\text{Iso} = \frac{\sum_{\text{trk}}^{\Delta R=0.3} p_T^{\text{charged hadron}} + \sum_{\text{ecal}}^{\Delta R=0.3} E_T^{\text{neutral hadron}} + \sum_{\text{hcal}}^{\Delta R=0.3} E_T^{\text{photons}}}{p_T} < 20\% \quad (4.1)$$

The Sums run over all particle flow objects namely charged and neutral hadrons or photons p_T within a cone with a radius $\Delta R = 0.3$ around the lepton.

4.2 Regions of Interest

Searches probing the limitations of the standard model often investigate very extreme kinematic regions like very high H_T and \cancel{H}_T regions. These are the most interesting regions for many models to find an excess above the SM expectation.

To distinguish between SM background events and signal events including new particles, the SM processes must be predicted as precisely as possible.

To validate that the background estimations are capable of predicting the background events, a control region is defined. This control region is selected according to the baseline cuts including high statistics while being dominated by SM events (the amount of expected signal events is negligible).

The cuts for the most sensitive regions are always chosen to be very extreme leading to a small amount of SM events. The search regions used by this analysis differ only by the H_T and \cancel{H}_T selection. All regions have been chosen to be exclusive in H_T and \cancel{H}_T to make them statistical independent for the limit setting procedure. Table 4.1 lists the baseline selection and all the search regions.

4.3 Data and simulated event samples

In 2011 the LHC and the CMS detector have performed extraordinary well resulting in a collected luminosity of 4.98 fb^{-1} . A suit of H_T and $H_T \cancel{H}_T$ cross-trigger was used to collect the data for this analysis. All datasets are reconstructed using `CMSSW_4_2_X`.

Tests and validation of the lost-lepton method were done on different simulated event samples, called Monte Carlo (MC) samples, listed in Tab. 4.2 which were reweighted according to the pileup distribution obtained from the collected 4.98 fb^{-1} of data. The background estimation was done on the 4.98 fb^{-1} of the full 2011 dataset listed in Tab. 4.3.

Table 4.1: This table lists all used regions (numbered from 1 to 14) defined by ranges in H_T and \cancel{H}_T .

	H_T (GeV)	\cancel{H}_T (GeV)
baseline	500...	200...
1	500...800	200 ...350
2	500...800	350 ...500
3	500...800	500 ...600
4	500...800	600 ...
5	800...1000	200 ...350
6	800...1000	350 ...500
7	800...1000	500 ...600
8	800...1000	600 ...
9	1000...1200	200 ...350
10	1000...1200	350 ...500
11	1000...1200	500 ...
12	1200...1400	200 ...350
13	1200...1400	350 ...
14	1400...	200 ...

Table 4.2: This table lists statistics of each used MC sample. The most important samples are the $t\bar{t}$ and W^\pm +jets.

Event name	sample name	amount of events [million]
$t\bar{t}$	TTJets_TuneZ2_7TeV-madgraph-tauola	59.6
W^\pm +jets	WJetsToLNu_300_HT_inf_TuneZ2_7TeV-madgraph-tauola	5.4
Z	DYJetsToLL_TuneZ2_M-50_7TeV-madgraph-tauola	36.3
QCD	QCD_Pt-15to3000_TuneZ2_Flat_7TeV_pythia6	11.0
WW	WW_TuneZ2_7TeV_pythia6-tauola	4.2
WZ	WZ_TuneZ2_7TeV_pythia6-tauola	4.3
ZZ	ZZ_TuneZ2_7TeV_pythia6-tauola	4.2

Table 4.3: 2011 7 TeV pp collision datasets used for the analysis. Total integrated luminosity is 4.98 fb^{-1} .

Dataset	Dataset run range	Lumi (fb^{-1})
/HT/Run2011A-May10ReReco-v1	160404–163869	0.22
/HT/Run2011A-PromptReco-v4	165088–167913	0.95
/HT/Run2011A-05Aug2011-v1	170249–172619	0.39
/HT/Run2011A-PromptReco-v6	172620–173692	0.71
/HT/Run2011B-PromptReco-v1	175832–180252	2.71
Total	160404–180252	4.98

5 The prediction of lost leptons from $t\bar{t}$ and $W^\pm + \text{jets}$ events

5.1 Concept of the lost-lepton background estimation

The by far most important fraction of events in the search region leading to e and μ with jets in the final state originates either from the decay of a $t\bar{t}$ where $t \rightarrow b + W^+$ ($\bar{t} \rightarrow \bar{b} + W^-$) or from a $W^\pm + \text{jets}$ event. Fig. 5.1 shows typical Feynman diagrams for such events. The involved W decays either directly to an $e + \nu_e$ or $\mu + \nu_\mu$ or via the intermediate state of a $\tau + \nu_\tau$. In the following only muons and electrons are meant by "leptons" if not stated otherwise.

The ν leaves the detector undetected leading to missing transverse energy. The lepton

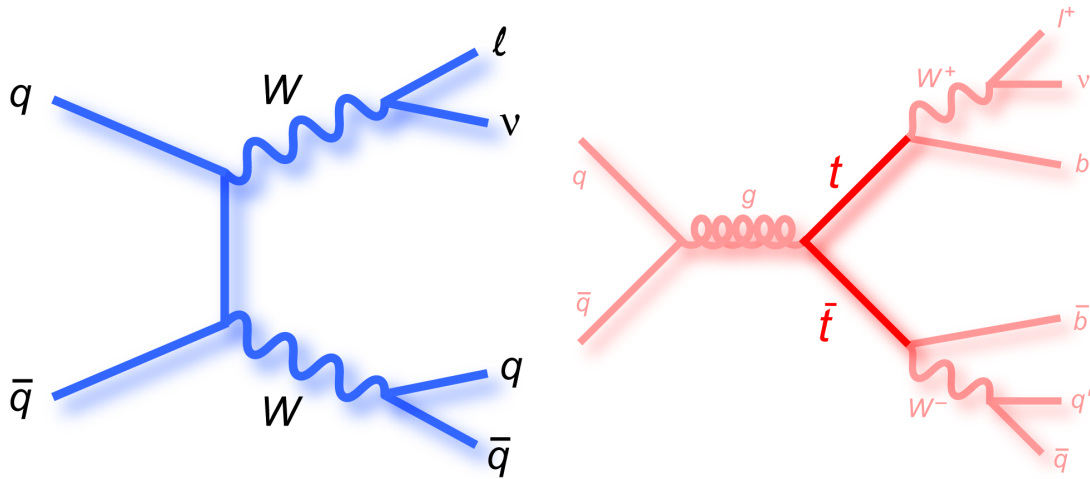


Figure 5.1: Feynman diagram for a typical $W^\pm + \text{jets}$ decay on the left and a $t\bar{t}$ decay on the right at the LHC [1].

veto defined in Sec. 4.1 removes only events if leptons are within the detectors acceptance and fulfill the reconstruction and isolation criteria. The lost-lepton background arises when the lepton veto fails to identify a prompt lepton.

The background is estimated by a muon control sample (CS) which is reweighted according to the lepton identification (in)efficiency of the detector. This idea holds when the event kinematics of the CS and the not detected leptons are similar, so that the background can be modeled by the CS. Extensive tests on simulated events have been performed to prove the methods capability of predicting lost leptons, see Sec. 5.5.

All plots in this section labeled "CMS Simulation", "CMS preliminary" or "CMS" have been done by me, made public by CMS and can be found on the public twiki web page [38].

5.2 The control sample

The control sample (CS) includes events which pass the same kinematic cuts as the event selection (see Sec. 4.1) but the lepton veto is inverted requiring exactly one well identified muon. The p_T of the muon is included in the H_T and \cancel{H}_T calculation.

A small contribution comes from $t\bar{t}$ decays to two leptons (dileptonic). These events enter the CS if only one lepton is lost. The case that one lepton is lost is twice as often than both are lost. The amount of lost leptons is therefore overestimated by a factor of two for the dileptonic decays. A selection on MC of events including one muon from dileptonic decays has been compared to the selection where two leptons are lost. The m_T cut discussed in Sec. 4.1 reduces the amount of dileptons in the CS to only 3% of the total CS. These 3% lead to an over-prediction of 1.5% of the total prediction. The prediction is corrected for this.

Another minor contribution arises from diboson event and single top. The contribution has been found to be less than 1.5% of the total CS. This contribution is covered within the assigned uncertainty (see Sec.5.8). Fig. 5.2 and Fig. 5.2 show the p_T , H_T and \cancel{H}_T distribution of the CS selected from simulated $t\bar{t}$ and W^\pm +jets events and data. Good agreement can be observed.

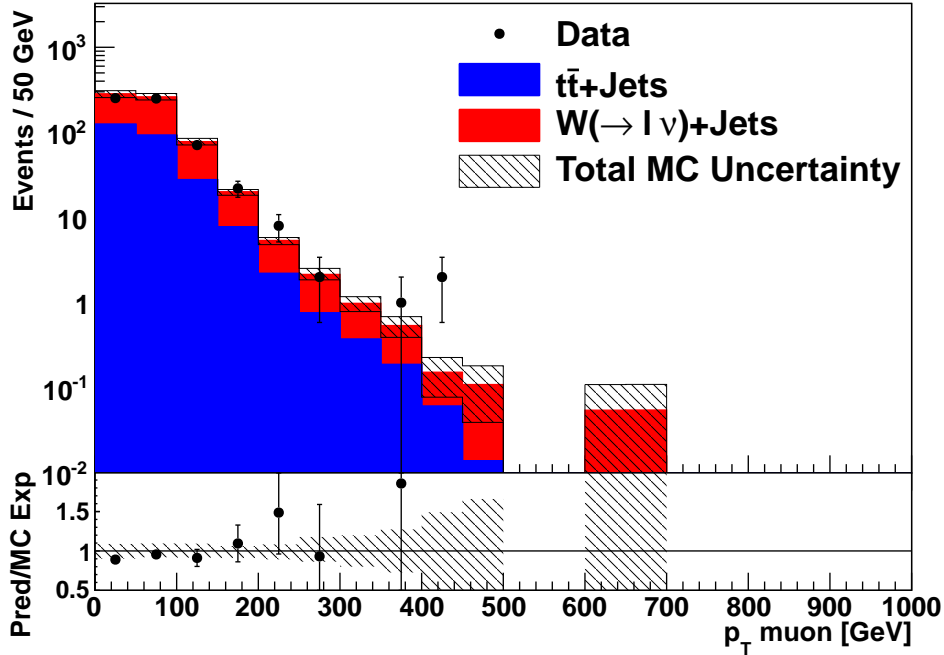


Figure 5.2: This plot shows a comparison of the μ control sample p_T spectrum selected on data corresponding to the full 4.98 fb^{-1} recorded 2011 and simulated $t\bar{t}$ and W^\pm +jets events referred to as MC.

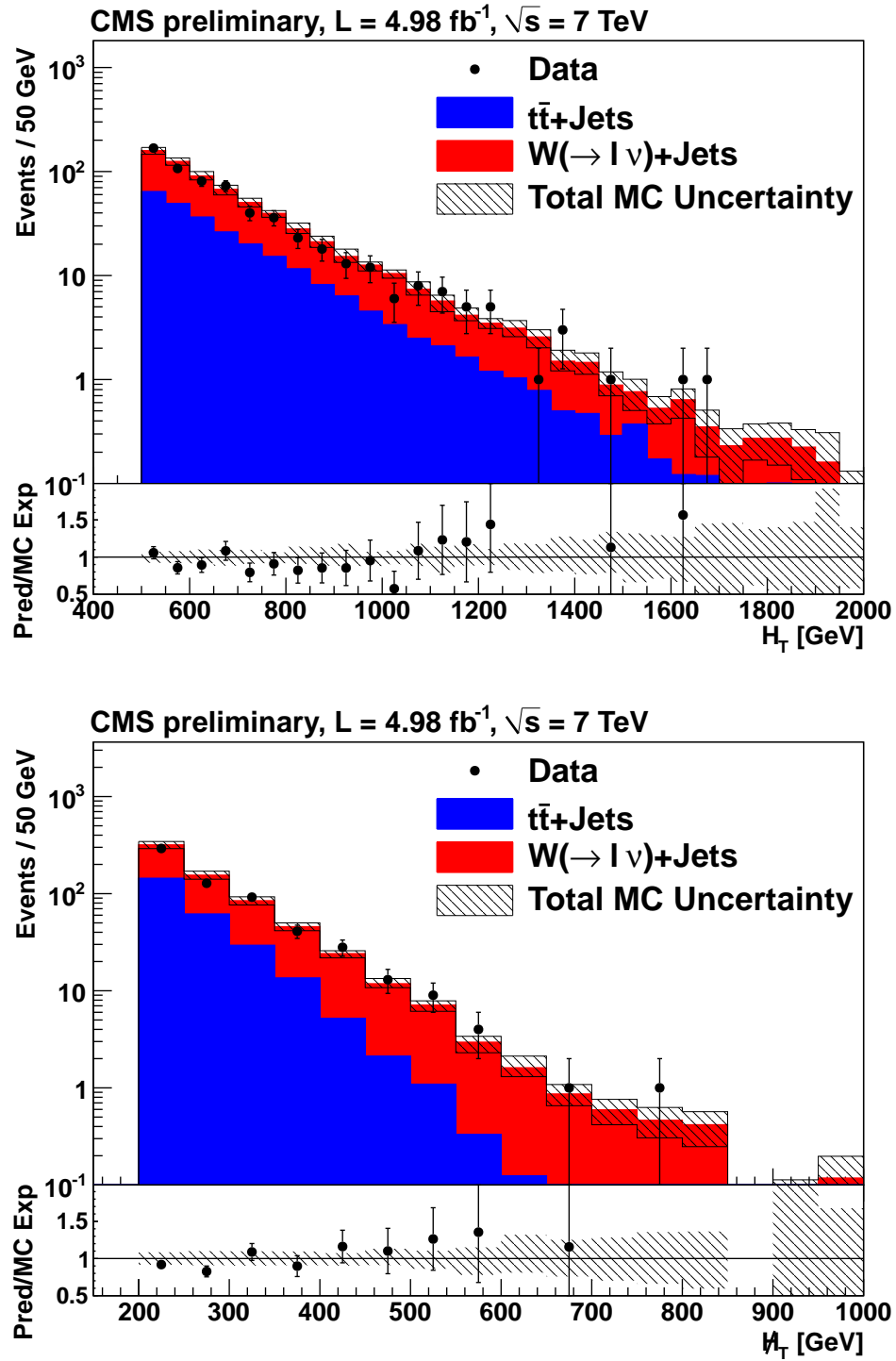


Figure 5.3: These figures show a comparison of the μ control sample for the H_T and H_T distribution selected on data corresponding to the full 4.98 fb^{-1} recorded 2011 and simulated $t\bar{t}$ and W^\pm +jets events.

5.2.1 Signal Contamination

Events involving physics beyond the standard model can contain jets, missing transverse momentum and leptons, in particular muons in the final state. Such events can enter the CS leading to an over estimation of the lost-lepton background. This is referred to as "signal contamination" of the CS.

For the SM background the muons in the CS are products of a W^\pm decay while this is generally not expected for signal events. The topology of the W^\pm decay can be used to distinguish between SM background and signal events. The transverse-mass-distribution (m_T) has shown to be a useful value to remove possible signal contamination of the CS.

$$m_T = \sqrt{2p_T(\mu)\cancel{E}_T(1 - \cos(\Delta\Phi))} \quad (5.1)$$

with $p_T(\mu)$ being the p_T of the muon in the CS, \cancel{E}_T the missing energy in the event and $\Delta\Phi$ being the angel between the $\vec{\cancel{E}}_T$ and the μ .

Fig. 5.4 shows the m_T for the CS selected on data and MC together with the LM5 cMSSM

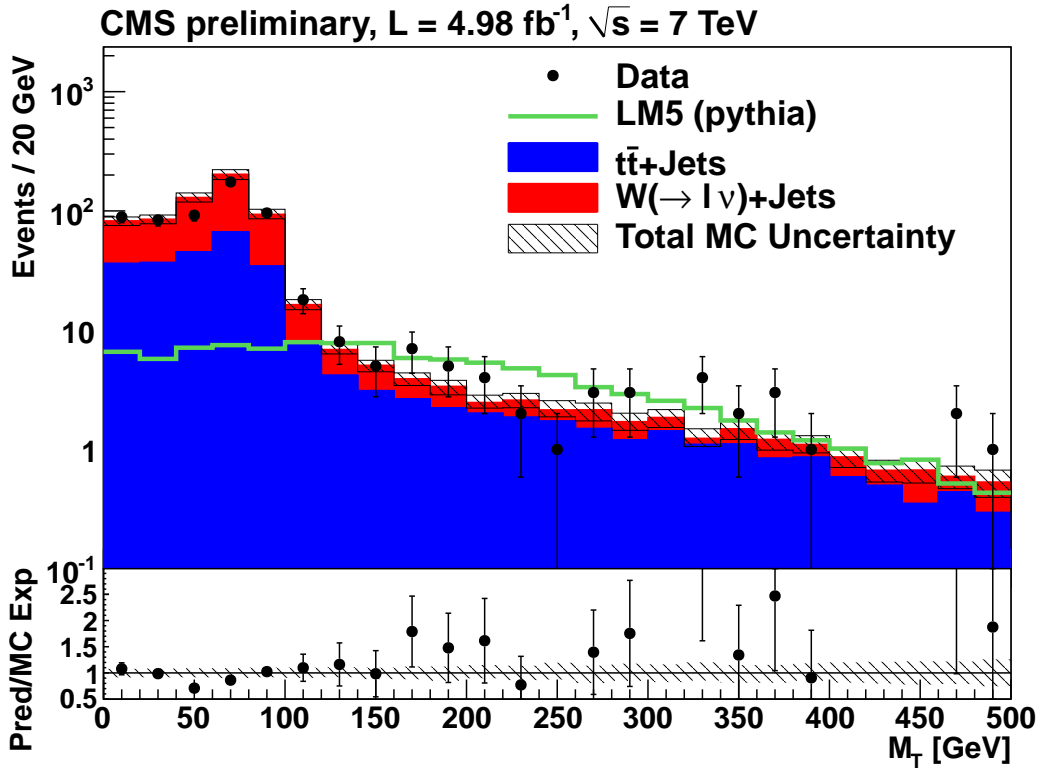


Figure 5.4: This plot shows the m_T distribution of the control sample in data, for simulated $t\bar{t}$ and W^\pm +jets events and for an example signal point (LM5). The m_T distribution of the CS steeply falls above 80 GeV for the SM process, where as the LM5 distribution is rather wide. (The legend description can be found in the caption of Fig. 5.2)

benchmark point. For the SM background events the transverse-mass-distribution rises up to the W^\pm mass of 80.4 GeV above which it steeply falls while a broad distribution is being observed for signal events (LM5).

A cut at 100 GeV to remove everything above has shown a good balance between Standard Model CS reduction and signal contamination rejection. Note that because of the detectors finite resolution of muon and jet p_T some cases have a m_T value higher than m_W ¹.

The efficiency, defined as the ratio of Standard Model CS events passing the cut to all Standard Model CS events, for the search regions and the baseline selection can be seen in Fig. 5.5. The error bars cover the statistical uncertainty of the used MC. A good efficiency of about 90% can be observed for all regions.

A constant correction factor of 10% together with an uncertainty of 4.0% is applied on data to correct for the removed Standard Model CS and cover for the variation of the cut efficiency.

Overall, possible signal contamination leading to an over estimation of the background and therefore a reduction of the sensitivity of the analysis to new particles has been reduced by the m_T cut, increasing the capability of the analysis of finding new physics.

5.2.2 Other SM background contributions

The main SM background contributing to lost-lepton CS arises as discussed from $t\bar{t}$ and W^\pm +jets events. However other processes can contribute by ending up in the CS. There are QCD events, ZZ or Z processes which can have the same signature and contribute to the background.

The samples listed in Tab. 4.2 have been used to study these backgrounds by selecting a control sample on the corresponding MC samples. Tab. 5.1 shows the amount of events for each of the other SM backgrounds scaled to the full luminosity of 4.98 fb^{-1} . No considerable amount of events has been found. An uncertainty of less than 3% is justified to cover for these SM background contributions and for possible other contributions which are expected to be magnitudes below the listed ones.

	Number of Events in the CS	\pm	ratio[%]
QCD	0	0	0
ZZ	0.04	0.02	0.0
Z	7.99	2.02	1.2
$Summe$	8.03	2.04	1.2
W^\pm +jets & $t\bar{t}$	658.20	5.00	100

Table 5.1: This table shows the amount of additional SM processes which add to the CS selected on MC compared to the selection from $t\bar{t}$ and W^\pm +jets events. The shown ratio is defined as SM background divided by the main background ($t\bar{t}$ and W^\pm +jets). All numbers are scaled to the full luminosity of 4.98 fb^{-1} .

¹Also the small amount of dileptonic $t\bar{t}$ decays lead to higher m_T .

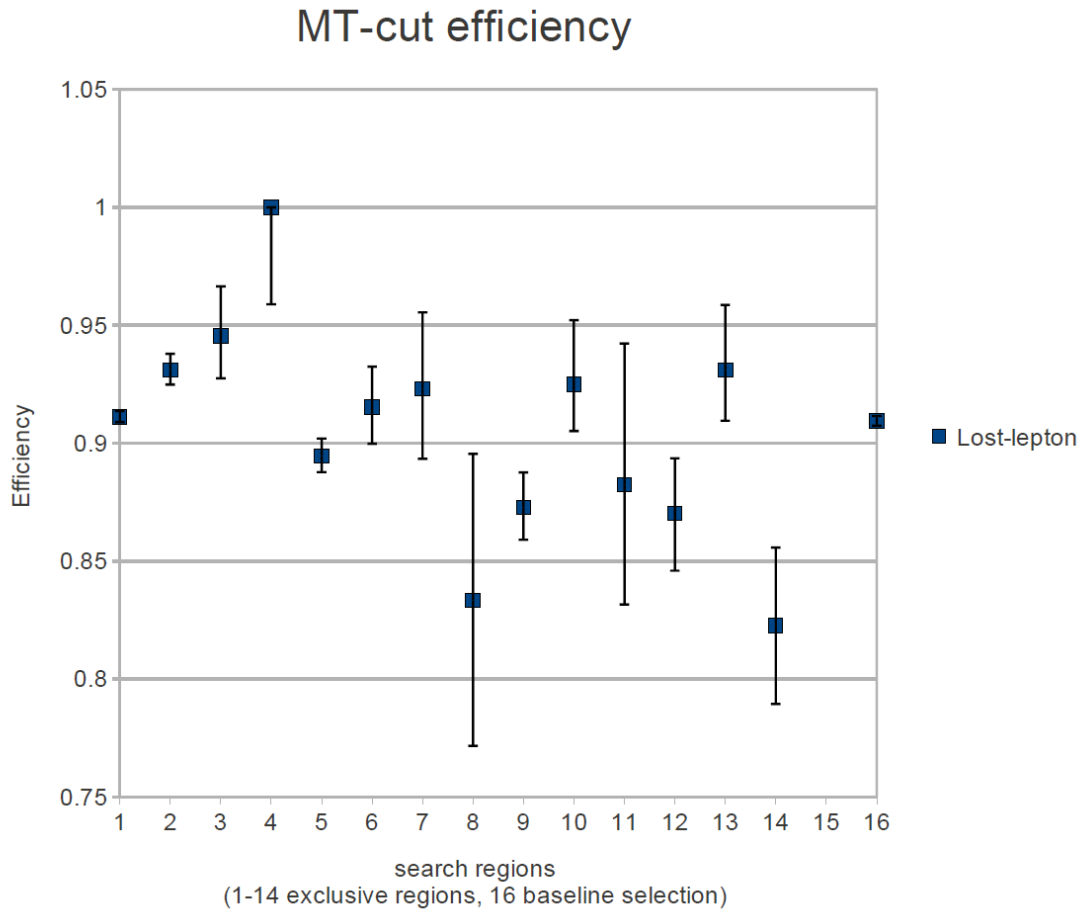


Figure 5.5: This plot shows the efficiency of the m_T cut for all exclusive regions (the numbering corresponds to the enumeration in Tab.4.1) for bin 1-14. Bin 16 shows the value for the baseline selection.

5.3 Predicting the lost electrons and muons

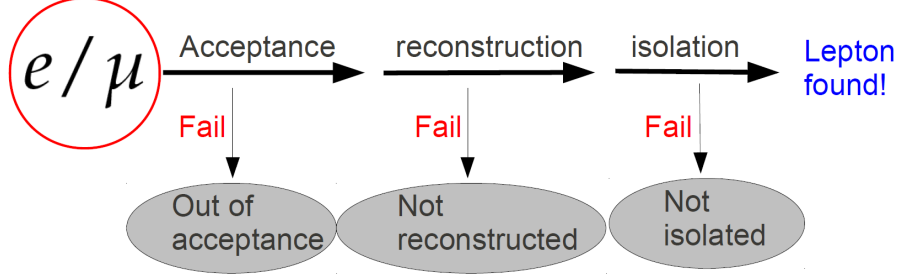


Figure 5.6: Visualization of the steps a muon has to take in order to enter the control sample

There are three steps a lepton has to take to be rejected by the lepton veto.

1. First it has to be within the detector acceptance.
2. The second step is the reconstruction.
3. The final step is the isolation criteria.

The CS is weighted according to each efficiency individually. Fig. 5.6 shows a chart of this three steps.

Since the control sample of well identified and isolated muons is used, one has to start predicting the three steps in reversed order.

Starting with modeling the not isolated muons followed by predicting the not reconstructed and finally the out of acceptance muons. To model the not isolated muons the CS is weighted according to:

$$!ISO^\mu = CS \cdot \frac{1 - \epsilon_{ISO}^\mu}{\epsilon_{ISO}^\mu} \quad (5.2)$$

with $!ISO^{\text{lepton}}$ being the applied weight and $\epsilon_X^{\mu/e}$ being the efficiency of the criteria X for the lepton.

The next step is to model the not reconstructed muons which is done by taking the muon isolation and reconstruction (in)efficiency into account. The weight is calculated according to the following equation:

$$!Reco^\mu = CS \cdot \frac{1}{\epsilon_{ISO}^\mu} \cdot \frac{1 - \epsilon_{Reco}^\mu}{\epsilon_{Reco}^\mu} \quad (5.3)$$

The last step in modeling the lost muons is to take also the muons into account which fall out of the detector acceptance. The weight has to include the isolation and reconstruction (in)efficiencies together with the out of acceptance efficiency:

$$!Acc^\mu = CS \cdot \frac{1}{\epsilon_{ISO}^\mu} \cdot \frac{1}{\epsilon_{Reco}^\mu} \cdot \frac{1 - \epsilon_{Acc}^\mu}{\epsilon_{Acc}^\mu} \quad (5.4)$$

The electrons are modeled using the same muon CS. This is valid since the decay of a W to a μ or e has according to the lepton universality the same probability [39]. All muon (in)efficiencies need to be taken into account before modeling the lost electrons resulting in more complex equations. The following equations are used to model the not isolated (Eq. 5.5), not reconstructed (Eq. 5.6) and the out of acceptance electrons (Eq. 5.7).

$$!ISO^e = CS \cdot \frac{1 - \epsilon_{ISO}^e}{\epsilon_{ISO}^\mu} \cdot \frac{\epsilon_{Reco}^e}{\epsilon_{Reco}^\mu} \cdot \frac{\epsilon_{Acc}^e}{\epsilon_{Acc}^\mu} \quad (5.5)$$

$$!Reco^e = CS \cdot \frac{1}{\epsilon_{ISO}^\mu} \cdot \frac{1 - \epsilon_{Reco}^e}{\epsilon_{Reco}^\mu} \cdot \frac{\epsilon_{Acc}^e}{\epsilon_{Acc}^\mu}. \quad (5.6)$$

$$!Acc^e = CS \cdot \frac{1}{\epsilon_{ISO}^\mu} \cdot \frac{1}{\epsilon_{Reco}^\mu} \cdot \frac{1 - \epsilon_{Acc}^e}{\epsilon_{Acc}^\mu} \quad (5.7)$$

The final equation to predict all lost leptons is:

$$\text{all lost leptons} = C \cdot \sum_{i=e,\mu} (!Iso^i + !Reco^i + !Acc^i) \quad (5.8)$$

with C being a correction factor consisting of the correction factor for the m_T cut efficiency discussed in Sec. 5.2.1, a small factor for di-leptonic events discussed in Sec. 5.2 and a "non-closure" factor discussed in Sec. 5.5.

5.4 Lepton Efficiencies

This chapter describes how the six efficiencies, used to weighted the CS, are obtained. The acceptance efficiency has been calculated from MC by comparing the amount of leptons fulfilling the acceptance criteria defined in Sec. 5.4.2 to all prompt leptons. This has been done for the baseline selection without the lepton veto for muons and electrons separately.

The isolation efficiencies, taken from [40], were obtained by a Tag&Probe method (Sec. 5.4.1) on the Z -Resonance. The efficiencies are parametrized in $\frac{p_{t,lep}}{p_{t,jet}}$, with $p_{t,lep}$ being the lepton and $p_{t,jet}$ being the p_T of the closest jet, and ΔR to the closest jet.

This is necessary since the lepton isolation depends strongly on the activity around the lepton (see Sec. 4.1) and the selection of the Z -Resonance has a different topology than the topology of the signal.

The reconstruction efficiencies are obtained from MC by calculating the ratio of generator leptons which can be matched to reconstructed leptons.

5.4.1 Tag&Probe method

Tag&Probe methods are well established methods to measure the efficiency of detectors to identify and isolate leptons. The idea is to take a well known process which has a good understood final state of two leptons and good understood background processes (a fit function is used to model the background from other processes).

For the here presented efficiencies the Z -resonance was used. The Z -boson can only decay to two leptons, two jets or two neutrinos. Therefore if one lepton is found another lepton of the same flavor must be in the event too.

The Tag&Probe method starts with a well identified "tag"-lepton. The tag-lepton has to pass tight identification cuts to make sure that it is a proper prompt lepton.

To leave other possible leptons in the event unbiased this tag-leptons are required to fire the trigger used for the sample selection.

Then another lepton ("probe"-lepton) in the event is selected without any isolation and, depending on the to be probed efficiency, suitable reconstruction criteria. When this lepton is found both are combined to the mass of the Z -Boson. Only events with a reconstructed mass between 60 and 120 GeV for muons and 70 to 110 GeV for electrons are used.

Then the isolation criteria or reconstruction criteria are applied to the probe-lepton, resulting in a fraction of probe-leptons passing and failing the isolation criteria. A function to each fraction is fitted modeling the Z -resonance together with the other (exponentially decreasing) background events. The ratio of the integral of both signal fits are used as isolation efficiency. The fitting uncertainty is included in the efficiency as uncertainty (more details can be found here [40]).

5.4.2 Leptons out of the detector acceptance

The out of detector acceptance leptons are defined as leptons with $p_T < 10\text{GeV}$ and muons with a $|\eta| > 2.4$ (electrons $|\eta| > 2.5$) which can not be detected (see Sec. 3). For the high $H_T > 500\text{ GeV}$ and $\cancel{H}_T > 200\text{ GeV}$ cuts the amount of leptons out of acceptance show no dependency on H_T or \cancel{H}_T . For muons an acceptance efficiency of 84% and for electrons

81% has been found².

5.4.3 Not reconstructed leptons

For the reconstruction efficiencies of the electrons the Tag&Probe method can not be used because the super clusters need to be cleaned by removing jets to have a significant purity of real electrons in the selection [40].

In order to still use the same parametrization as for the isolation efficiencies the reconstruction efficiencies are obtained from MC. A conservative estimate of 9% uncertainty is applied on the total prediction. In principle the μ could be calculated with the Tag&Probe method.

Previously [40] the reconstruction efficiencies had been done with a Tag&Probe method on data on the Z -Resonance with the parametrization of the efficiencies in $\frac{p_{t,lep}}{p_{t,jet}}$ and η . The prediction with the old efficiencies show a clear systematic under-prediction which is caused by the deficiency of the η parametrization to account for the kinematic differences between the Z -Boson resonance and the search regions.

As explained above (see Sec. 5.4) it is not possible to use a parametrization as a function of ΔR to the closest jet in the Tag&Probe method for the electrons, forcing the use of MC.

Fig. 5.7 shows a comparison of the closure tests for the prediction with the old efficiencies (right) and the new prediction (left). A clear under-prediction can be observed for the old efficiencies while the new efficiencies show a very good closure.

Fig. 5.8 shows the used electron and μ reconstruction efficiencies.

²The H_T and \cancel{H}_T distribution for the out of acceptance leptons can be found in Fig.5.15.

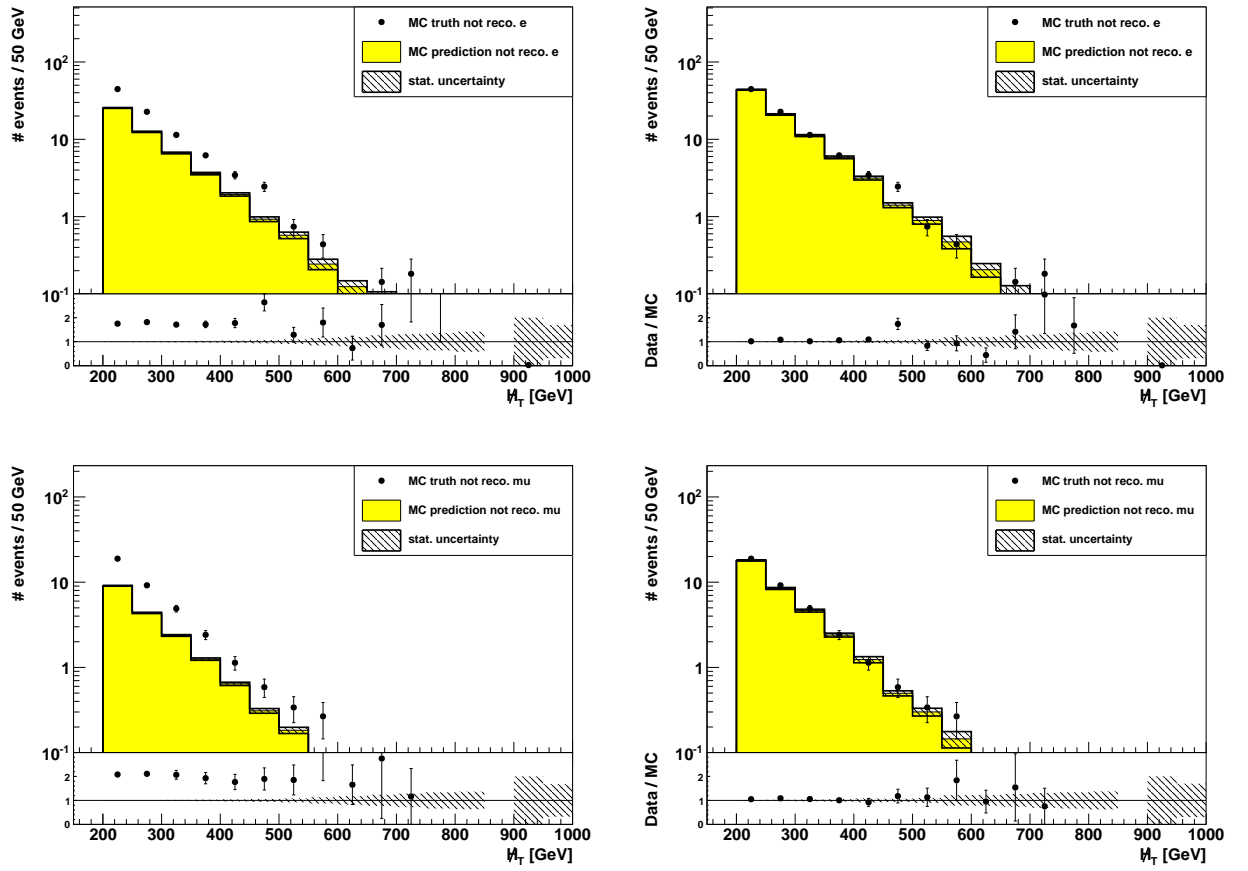


Figure 5.7: These plots show the MC closure ($t\bar{t}$ and W^\pm +jets combined) for not reconstructed electrons (upper two plots) and muons (lower two plots). On the left side for the old efficiencies binned in $\frac{p_{t,lep}}{p_{t,jet}}$ and η and on the right side with the new in lepton p_T and ΔR binned efficiencies.

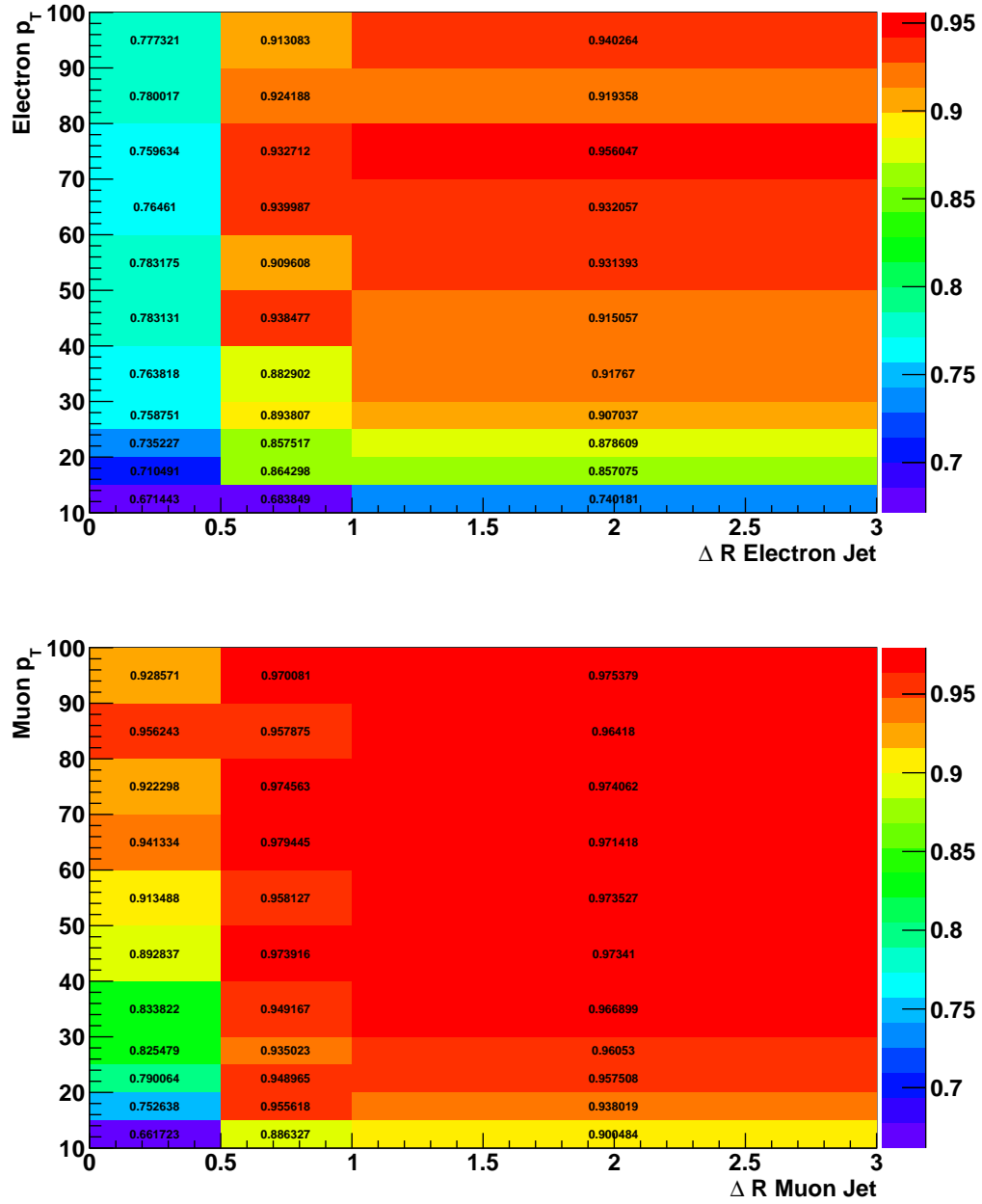


Figure 5.8: These plots show the electron and μ reconstruction efficiencies obtained from MC.

5.4.4 Not isolated leptons

When a lepton is reconstructed it also has to fulfill the isolation criteria to be identified as a prompt lepton. The applied isolation criteria are discussed in Sec. 4.1.

Leptons show a higher isolation dependency on their p_T and angular distance relative to the closest jet. Leading to the chosen efficiency parameterization in $\frac{p_{t,lep}}{p_{t,jet}}$ and ΔR to the closest jet. Especially for ΔR below 0.5 rad and low p_T the efficiencies decrease strongly. To achieve as much accuracy as possible the ΔR binning has been optimized. However the statistics of the Z -sample are very limited in very small ΔR . Fig.5.9 shows the isolation efficiencies for electrons and μ .

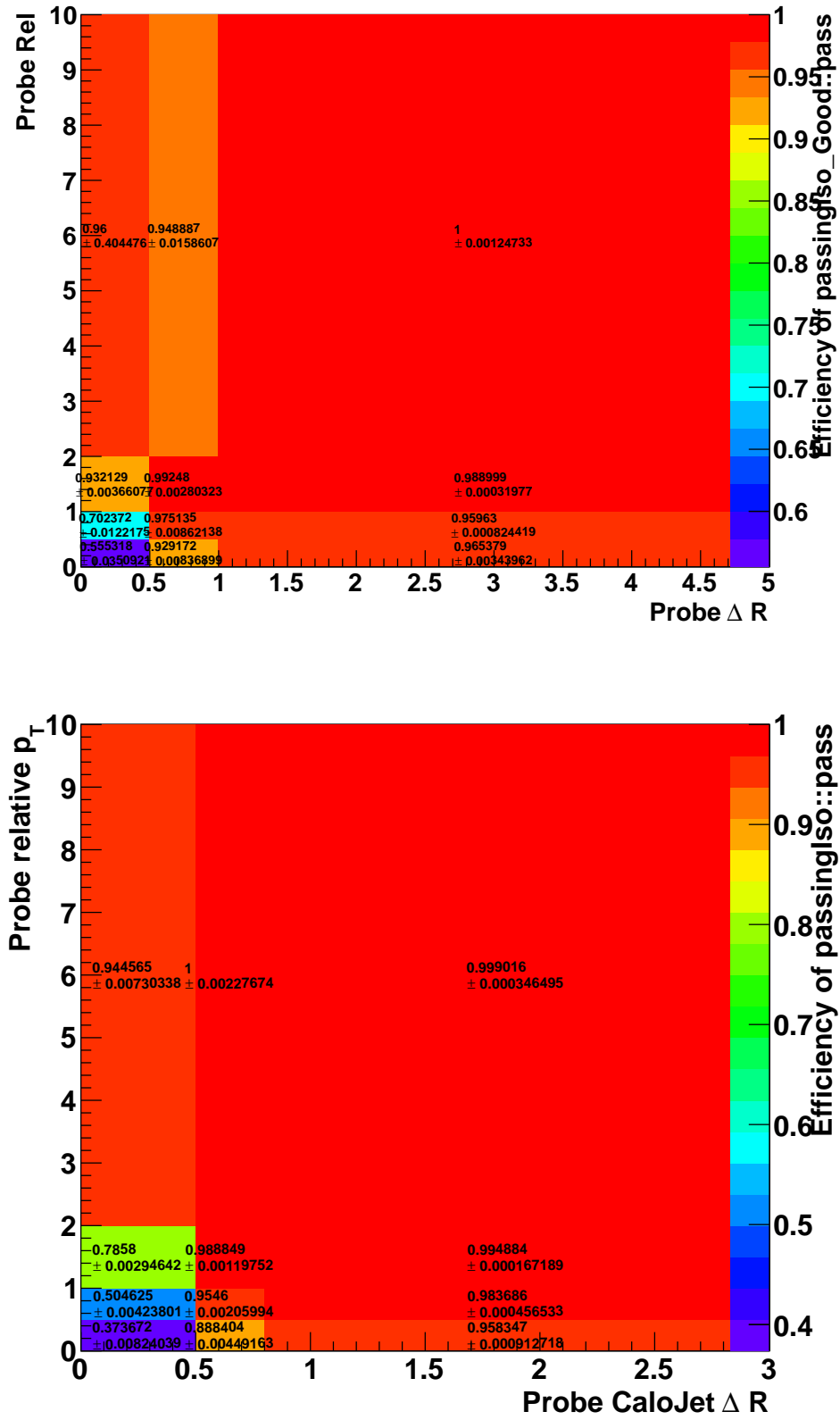


Figure 5.9: These plots show the electron and μ isolation efficiencies calculated with a Tag&Probe method.

5.5 Closure tests and prediction on data

Closure tests are a useful instrument of validating data driven methods on MC. For background estimations the prediction based on the MC control sample, labeled Data-driven Prediction from MC, is compared to the expected lost-leptons from MC, labeled MC expectation, in the signal region. Only statistical uncertainties are applied, since systematic uncertainties cancel within such a closure test.

One basic assumption of this method is that the topology of the CS and the signal sample do not differ considerable. The main search variables H_T and \cancel{H}_T along with the number of primary vertices (see Sec. 5.6) are investigated to validate this assumption.

The closer test for the H_T and \cancel{H}_T can be seen in Fig. 5.10. Good agreement in shape can be observed. Tab. 5.2 contains the numbers of the Data-driven prediction on MC events compared to MC expectation for $t\bar{t}$ and W^\pm +jets separately for the baseline selection. Also here good agreement can be observed. Despite a statistical significant discrepancy for the not reconstructed muons for W^\pm +jets and the not isolated muons for $t\bar{t}$, leading to an observed 4% underestimation, called non-closure, for which a correction factor is applied on data, the closure tests show that the topology of the events including lost leptons and the CS events agree well and that the assumption of similar topologies is valid for the baseline selection. The observed underestimation is discussed in the following.

Fig. 5.12 and Fig. 5.13 show the closure test for H_T and \cancel{H}_T for $t\bar{t}$ and W^\pm +jets sepa-

	$t\bar{t}$ expectation	$t\bar{t}$ predic.	W^\pm +jets expectation	W^\pm +jets predic.
μ , out of acceptance	51.1 ± 0.9	47.7 ± 0.4	79.6 ± 2.0	80.3 ± 0.9
μ , not reconstructed	16.6 ± 0.5	17.4 ± 0.3	18.3 ± 0.9	15.7 ± 0.3
μ , not isolated	34.6 ± 0.7	27.1 ± 0.6	25.9 ± 1.1	25.9 ± 1.1
e , out of acceptance	57.1 ± 0.9	55.5 ± 0.5	88.4 ± 2.1	90.8 ± 1.1
e , not reconstructed	35.4 ± 0.7	35.3 ± 0.4	50.1 ± 1.5	46.1 ± 0.7
e , not isolated	28.5 ± 0.6	21.0 ± 0.4	21.5 ± 1.0	21.2 ± 0.6
total	219.2 ± 1.8	204.1 ± 2.3	285.0 ± 3.7	280.0 ± 4.0

Table 5.2: This table shows the prediction on MC vs the expected events from MC. The numbers are scaled to 4.98 fb^{-1} .

rately. For W^\pm +jets both the \cancel{H}_T and H_T distribution agree well in shape. For $t\bar{t}$ the H_T distribution agrees also well but the \cancel{H}_T distribution shows an increasing under-prediction. Further closer tests have been done for the $t\bar{t}$ \cancel{H}_T distribution separately for not isolated, not reconstructed or out of the detector acceptance leptons.

The observed increasing under-prediction arises from the contribution of not isolation leptons and is passed to the other contribution since they also depend on the muon isolation efficiency (see Sec. 5.3).

This observation can be understood by considering the boost of the $t\bar{t}$ system at larger \cancel{H}_T . The increasing boost of the top quarks leads to a shrinking angular distance, ΔR , between the b -jet and the W . The final decay products, the lepton and the ν , are also boosted resulting in an increased \cancel{H}_T and smaller angular distance ΔR between the lepton and the b -jet. The under-prediction arises now since the isolation efficiencies decrease strongly with ΔR approaching 0 and as stated in Sec. 5.4.1 it is not possible to parametrize the

binning of the efficiencies ΔR any smaller. This incapability of the method to account for this extreme boosted systems with this very small ΔR is unavoidably and results in the observed increasing non-closure with increasing $\#_{\text{T}}$.

For the W^\pm +jets sample a similar dependency is not expected because there is no correlation between $\#_{\text{T}}$ and ΔR .

This well understood systematic under-prediction justifies the correction factor of 4% applied on data together with an additional uncertainty, introduced in Sec. 5.8, covering this dependency and other possible remaining differences in the closure, eg. the observed non-closure for the not reconstructed muons in the W^\pm +jets sample.

Fig. 5.15 shows the $t\bar{t}$ and W^\pm +jets combined closure test for the out of acceptance and not reconstructed fraction for electrons and muons separately. Together with the numbers from Tab. 5.2 one can observe good agreement for the not reconstructed and out of acceptance contribution.

Since it is not possible to separate the lost-lepton background from the other backgrounds, equivalent closure tests on data can not be done. Instead the μ CS from MC and data, and the prediction on data and MC are compared, as can be seen in Fig. 5.2 and Fig. 5.11. For both distributions a good agreement in shape can be observed. However both the control sample and the prediction show a significant difference (see Tab. 5.3) but the idea of data-driven background estimation is to be independent from MC. The observed differences are expected to origin from deficiencies in the MC simulation.

Tab. 5.3 contains the event yields on data, the Data-driven Prediction from MC and the MC Expectation. The prediction for the different search regions on data (defined in Sec. 4.1) including all systematics uncertainties (discussed in Sec. 5.8) are shown in Tab. 5.4.

Table 5.3: This table contains the final event yield for the lost-lepton background for the baseline selection on data and Data-driven Prediction from MC together with MC Expectation³. All uncertainties are included for the prediction on data. For the MC Expectation jet energy scale and luminosity uncertainties are applied and for the prediction on MC only statistical uncertainties are included.

	Pred.	Stat. Error	Tot. Sys.
prediction on data	453.5	± 26.3	+52.5 -53.4
MC Expectation	545.8	± 4.5	+50.4 -51.1
Data-driven Prediction from MC	524.1	± 5.0	

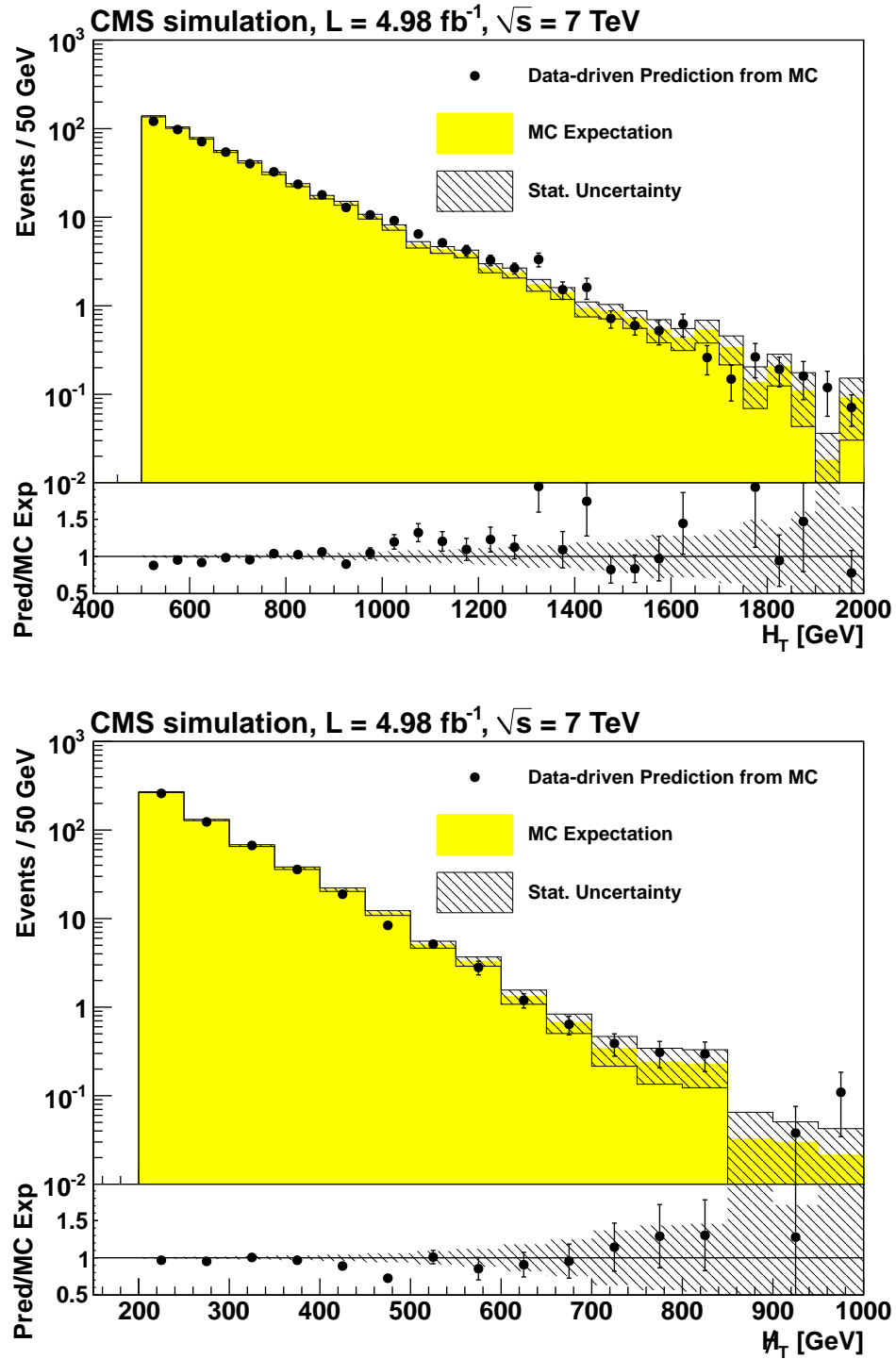


Figure 5.10: These plots show the closure test for the H_T and $\#H_T$ baseline selection for the total lost-lepton background. The estimated lost-leptons are called Data-driven Prediction from MC, which refers to $t\bar{t}$ and W^\pm +jets events combined and the observed lost-leptons are referred to as MC expectation.

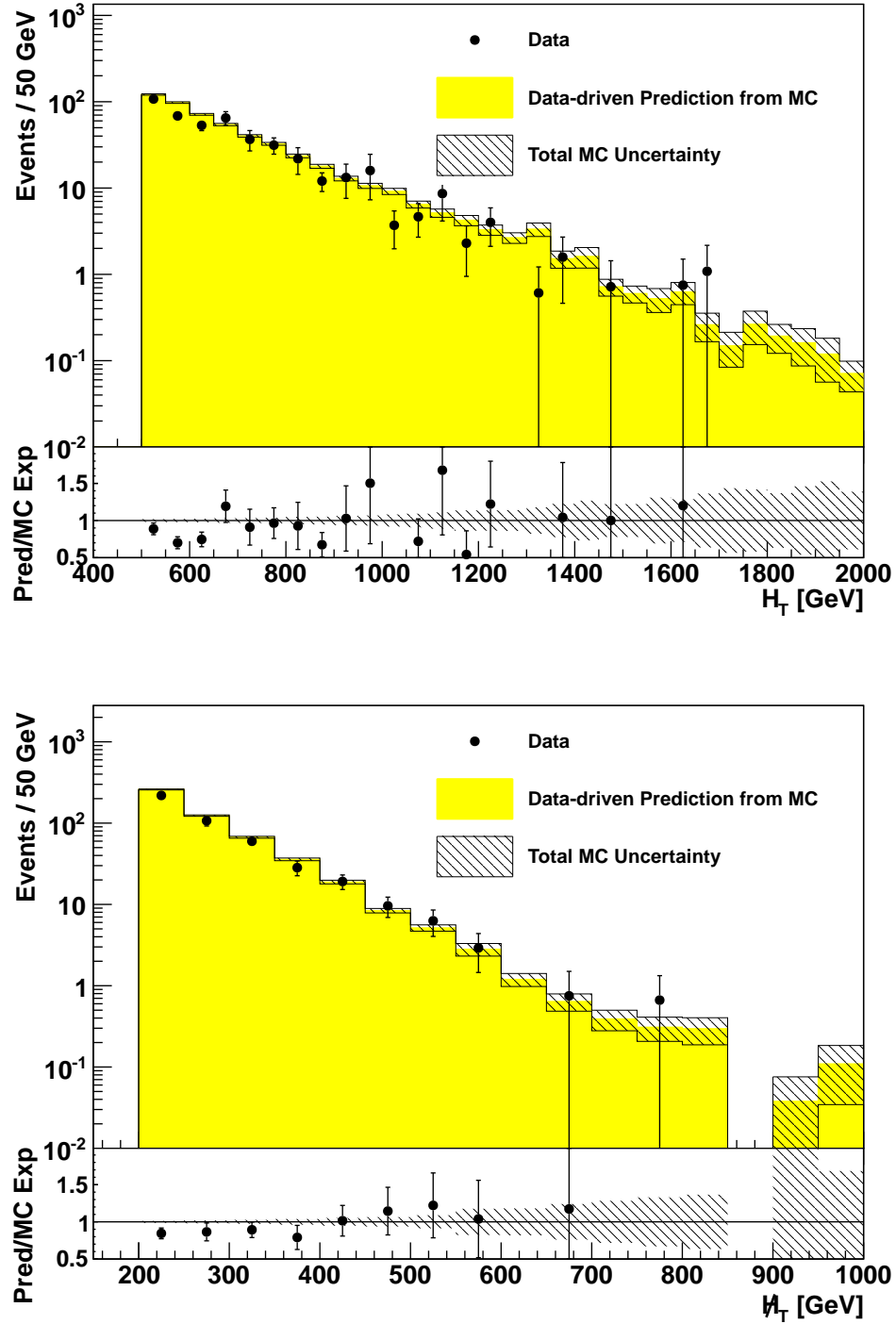


Figure 5.11: Comparison of the prediction on data vs. the prediction on MC ($t\bar{t}$ and W^\pm +jets combined) for the H_T (on the right) and the \cancel{H}_T (on the left) distribution. For the data prediction all uncertainties are shown while for the MC prediction only statistical uncertainties are shown. The shapes agree well within the uncertainties.

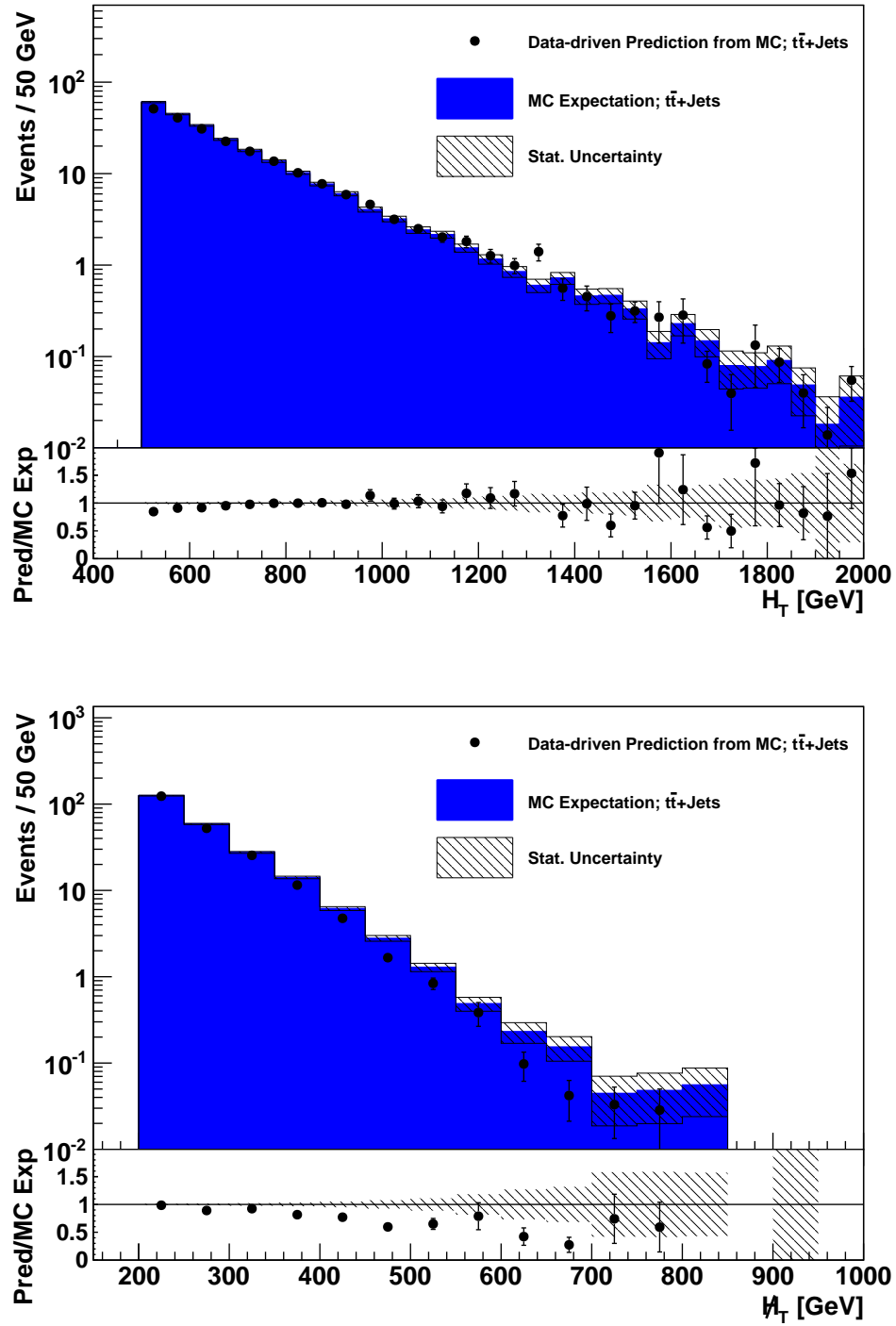


Figure 5.12: This plots show the closure test of the Data-driven Prediction from MC and the MC expectation for the H_T and $\#H_T$ distribution for $t\bar{t}$ simulated events. Good agreement of the shape as well as the ratio can be seen. Only the $\#H_T$ distribution shows a significant discrepancy.

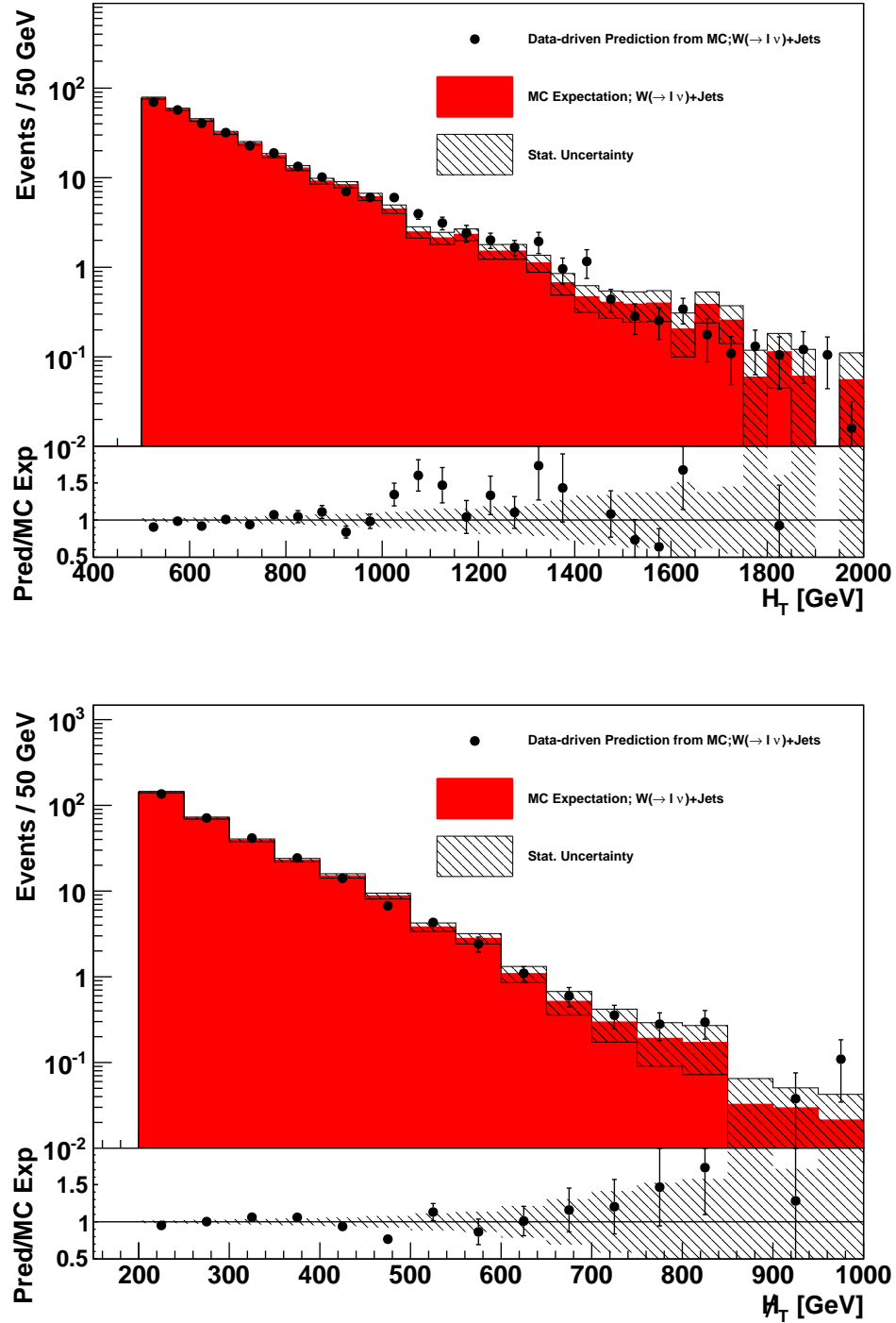


Figure 5.13: This plots show the closure test of the Data-driven Prediction from MC and the MC expectation for the H_T and $\#H_T$ distribution for W^\pm +jets simulated events. Good agreement of the shape as well as the ratio can be seen.

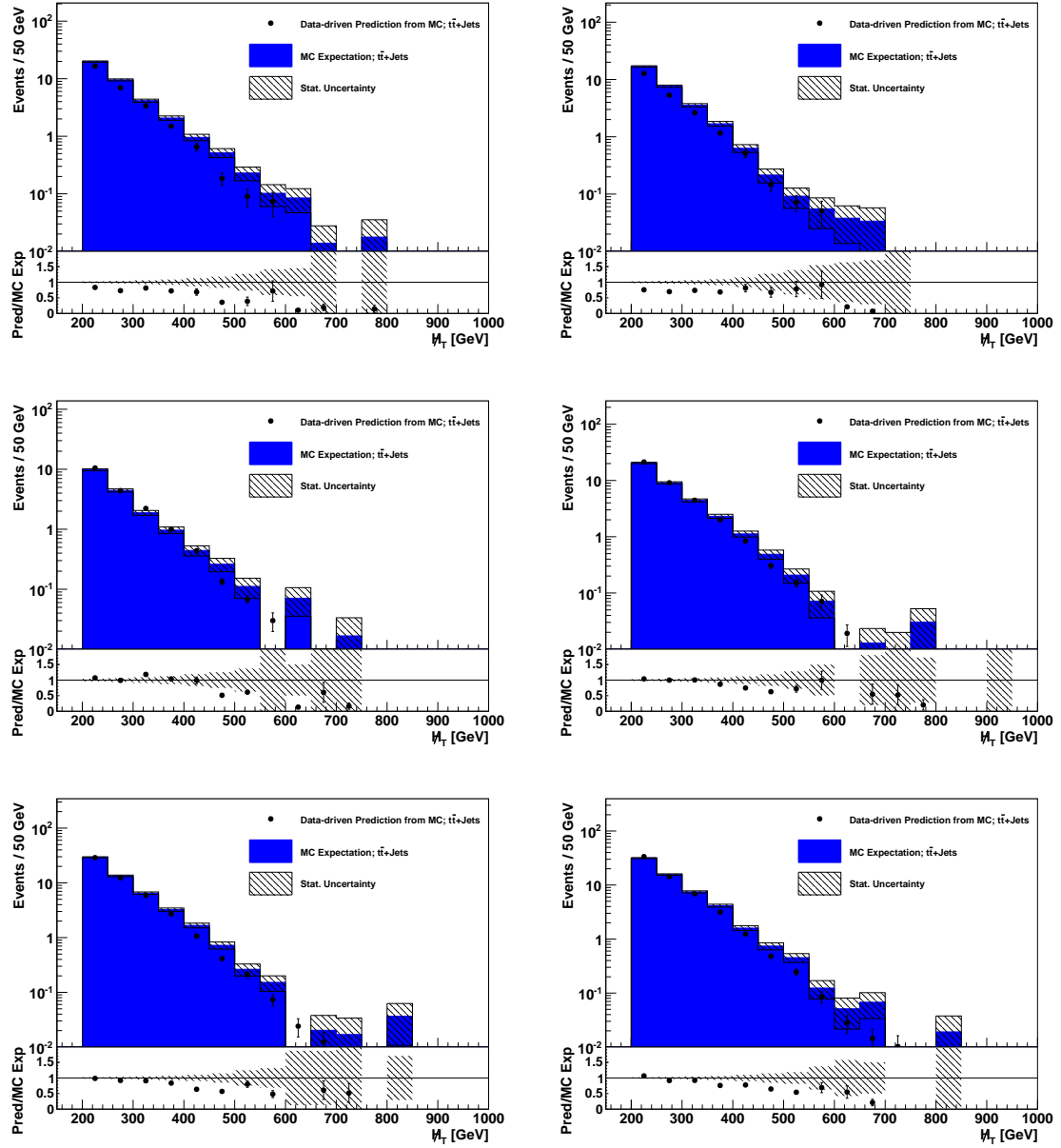


Figure 5.14: This plots show the closure tests for $t\bar{t}$ events separated for the not isolated (top), not reconstructed (middle) and out of acceptance fraction (bottom). Good agreement for the shape can be observed. However, an increasing under-prediction can also be seen. The legend description can be found in the caption of Fig. 5.12.

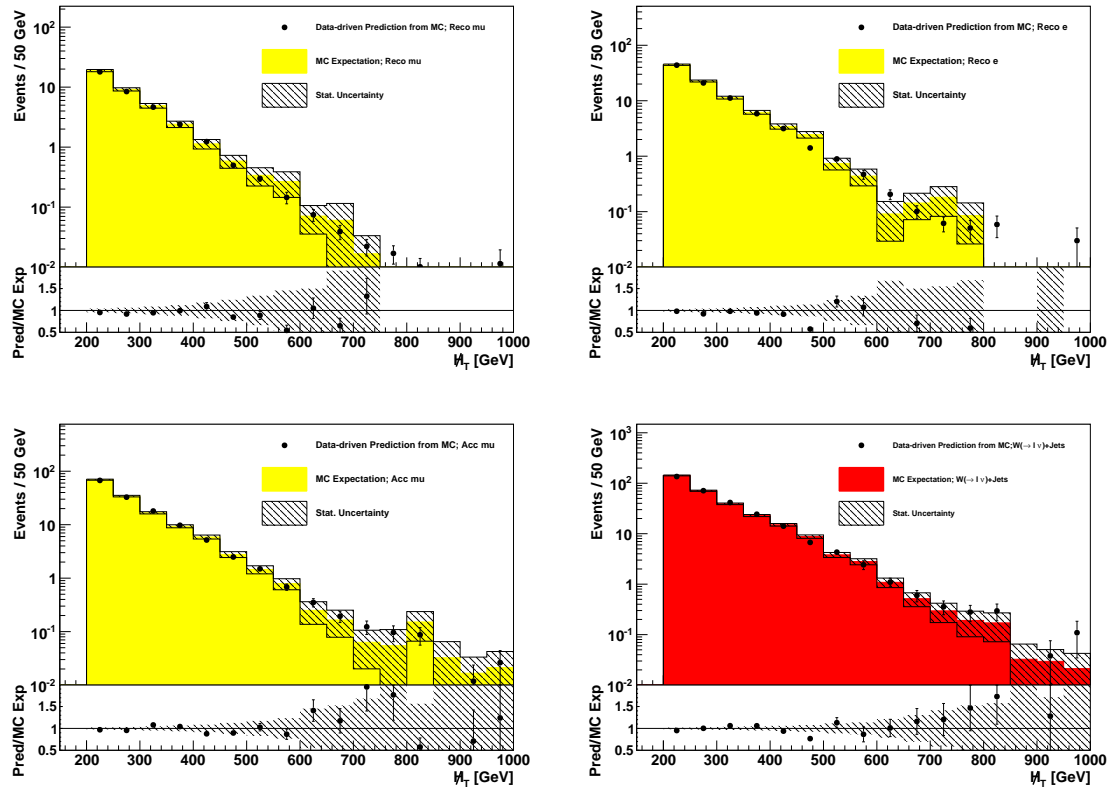


Figure 5.15: The upper two plots show the closure test for the not reconstructed muon on the left and for electrons on the right for $t\bar{t}$ and W^\pm +jets combined. On the bottom the same is shown for the out of acceptance background contribution. The legend description can be found in the caption of Fig. 5.12.

Table 5.4: Final event yield for the lost-lepton background for the exclusive search regions. The numbers are for the full luminosity of 4.98 fb^{-1} .

H_T (GeV)	$\#_T$ (GeV)	Pred.	Stat.	μ iso eff	MHT fit	elec. iso eff	syst. eff	acc	CS conta- mination	MTWcut	Tot. Sys.
baseline		471.6	27.3	2.6	21.4	+2.7 -2.7	47.2	16.2	+0.0 -14.1	+21.8 -19.6	+58.6 -59.5
500...800	200 ... 350	323.7	21.9	1.6	14.8	+1.6 -1.6	31.1	10.8	+0.0 -9.3	+14.4 -12.9	+40.3 -40.9
500...800	350 ... 500	47.4	6.1	0.1	3.9	+0.2 -0.2	4.6	1.8	+0.0 -1.4	+2.1 -1.9	+6.8 -6.8
500...800	500 ... 600	4.9	2.0	0.0	0.7	+0.0 -0.0	0.5	0.2	+0.0 -0.1	+0.2 -0.2	+0.9 -0.9
500...800	600 ...	0.8	0.8	0.0	0.2	+0.1 -0.1	0.1	0.0	+0.0 -0.0	+0.0 -0.0	+0.2 -0.2
800...1000	200 ... 350	57.2	13.4	0.6	2.6	+0.5 -0.5	5.5	1.6	+0.0 -1.6	+2.5 -2.3	+7.1 -7.2
800...1000	350 ... 500	5.2	2.1	0.0	0.4	+0.0 -0.0	0.5	0.2	+0.0 -0.2	+0.2 -0.2	+0.8 -0.8
800...1000	500 ... 600	2.3	1.3	0.0	0.3	+0.0 -0.0	0.2	0.1	+0.0 -0.1	+0.1 -0.1	+0.4 -0.4
800...1000	600 ...	0.7	0.7	0.0	0.1	+0.0 -0.0	0.1	0.0	+0.0 -0.0	+0.0 -0.0	+0.2 -0.2
1000...1200	200 ... 350	13.0	3.3	0.0	0.6	+0.1 -0.1	1.3	0.5	+0.0 -0.4	+0.6 -0.5	+1.7 -1.7
1000...1200	350 ... 500	4.7	4.1	0.0	0.4	+0.0 -0.0	0.5	0.1	+0.0 -0.1	+0.2 -0.2	+0.7 -0.7
1000...1200	500 ...	1.5	1.1	0.0	0.3	+0.0 -0.0	0.1	0.1	+0.0 -0.0	+0.1 -0.1	+0.3 -0.3
1200...1400	200 ... 350	4.0	1.9	0.0	0.2	+0.0 -0.0	0.4	0.1	+0.0 -0.1	+0.2 -0.2	+0.5 -0.5
1200...1400	350 ...	2.2	1.3	0.0	0.2	+0.0 -0.0	0.2	0.1	+0.0 -0.1	+0.1 -0.1	+0.3 -0.3
1400...	200 ...	2.6	1.5	0.0	0.2	+0.0 -0.0	0.3	0.1	+0.0 -0.1	+0.1 -0.1	+0.4 -0.4

5.6 Pileup dependency studies

During the year 2011 the instantaneous luminosity increased. A consequence is that the so called pileup has increased. Pileup is defined as the amount of additional, usually soft, interactions per bunch crossing leading to additional primary vertices. Albeit this analysis is only interested in the hard interaction with large energy transfer, other interactions lead to additional activity and energy deposition in the detector which can interfere with the reconstruction of leptons and jets.

A good measurable quantity related to pileup is the number of primary vertices. The amount of primary vertices is proportional to the additional energy introduced by pileup events. Studies have been performed to investigate the possible dependence of the lost-lepton background estimation.

Possible sensitivity of this analysis on pileup is expected for the isolation or reconstruction efficiency. For the isolation criteria (see Eq. 4.1 and Sec. 4.1) the amount of momentum in the ECAL, HCAL and tracker close to the lepton is crucial. When pileup increases more particles are produced and the isolation efficiency is expected to decrease if the energy deposited by pileup is large compared to the energy of the leptons and jets.

Closure test in the number of vertices have been done for $t\bar{t}$ and W^\pm +jets separately (see Sec. 5.3) and closer tests for electrons and μ separately. The closure of the full MC reweighted to the full 2011 pileup scenario extracted from data is shown in Fig. 5.16. No dependency on the number of vertices can be observed. Plot 5.17 shows the the closure test for the number of primary vertices for the not isolated electrons and muons for $t\bar{t}$ and W^\pm +jets separately. If any of the estimations would depend significantly on pileup an increasing under-prediction would be expected with increasing number of vertices. The samples for both electrons and muons show no such dependency, thus the isolation is not affected considerably by the pileup here studied. For the out of acceptance leptons no dependency is expected which is demonstrated in Fig. 8.2).

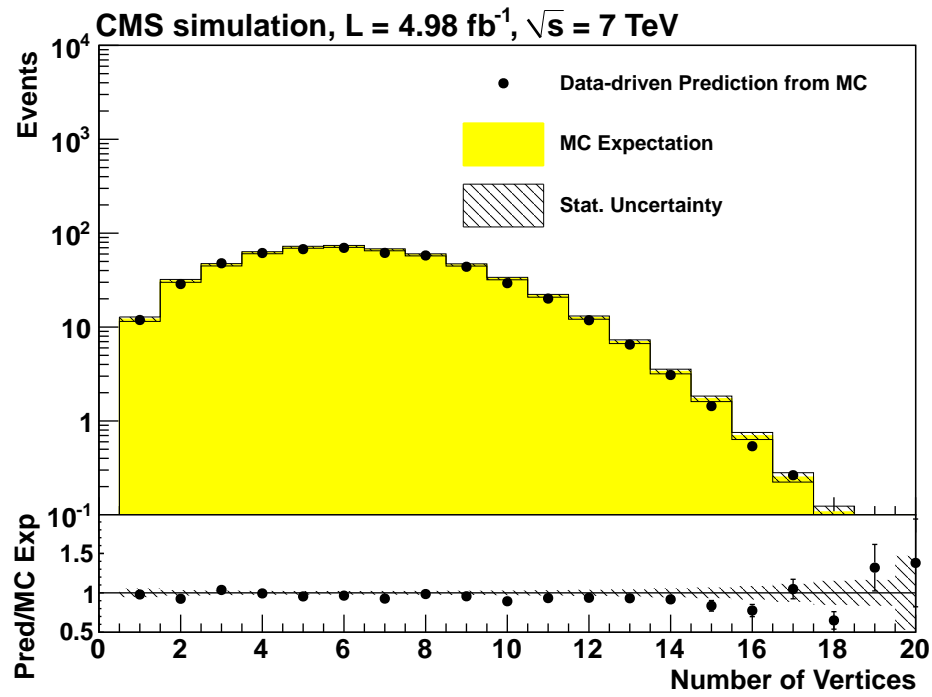


Figure 5.16: This plot shows the closure test for the $t\bar{t}$ and W^\pm +jets MC combined as a function of the number of primary vertices. The MC was reweighted according to the full 2011 pileup scenario. The legend description can be found in the caption of Fig. 5.10

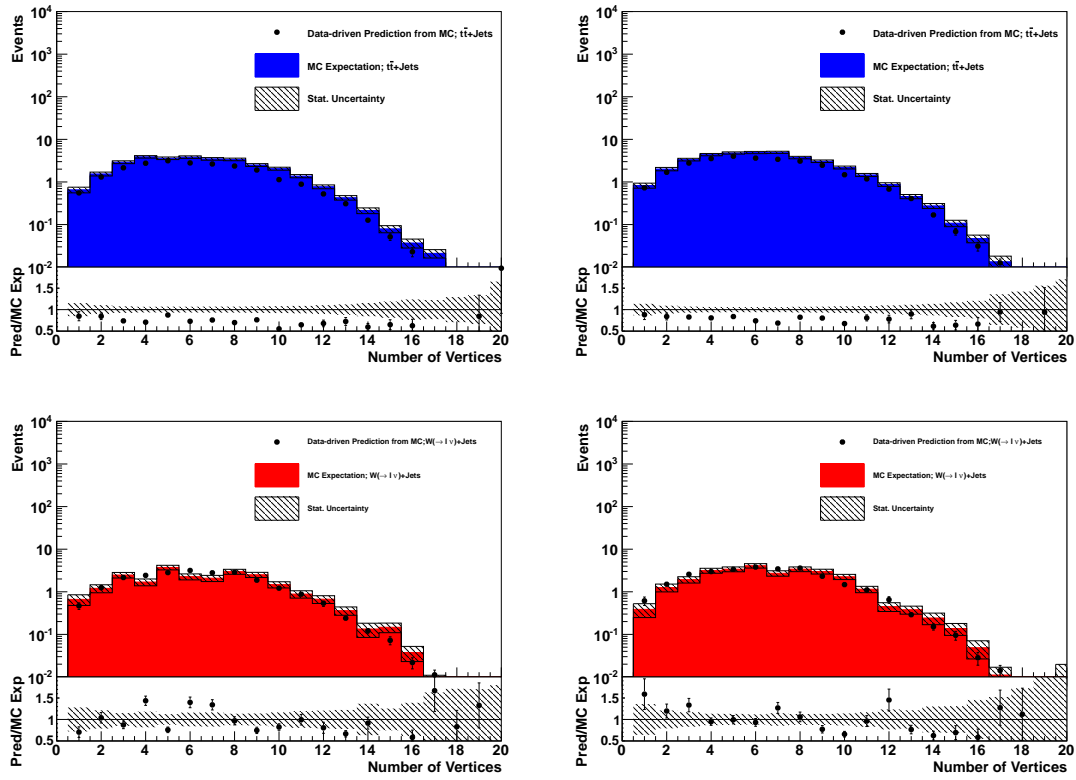


Figure 5.17: These plots show the closure test for the number of primary vertices separated for not isolated muons (left) and not isolated electrons (right), for $t\bar{t}$ (top), and W^\pm +jets (bottom). The method shows no dependency on the number of vertices neither for $t\bar{t}$ nor for W^\pm +jets events. The legend description can be found in the caption of Fig. 5.12.

The same studies were done to check if the reconstruction efficiencies have any pileup dependency. Fig. 5.18 shows a similar closure test for the not reconstructed muons and electrons, again no dependency on increasing pileup is being observed. For the out of

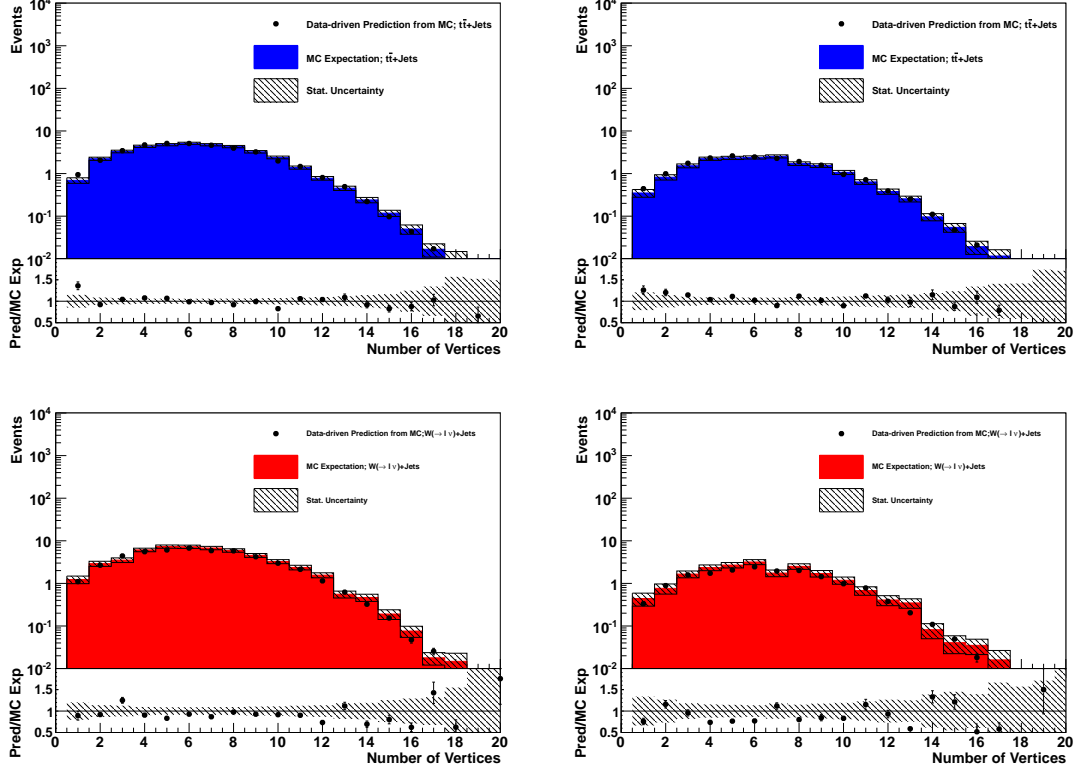


Figure 5.18: The two upper plots show the closure test for the not reconstructed electrons (right) and muons (left) for $t\bar{t}$ as the number of vertices while the two lower plots show the same distribution but for the W^\pm +jets sample. The legend description can be found in the caption of Fig. 5.12.

acceptance fraction no pileup dependency is expected. The p_T of the muons and electrons does not depend on the activity in the detector and also the amount of leptons out of the geometrical acceptance of the detector is not influenced by pileup.

As is shown and discussed above no contribution of the prediction shows any dependency on the number of vertices. The isolation criteria is very loose with a small cone and the selection requires already high energy. This justifies the statement that for the pileup here studied reaching out to about 16 number of vertices with reasonable statistics the lost-lepton background prediction is not significantly influenced by pileup.

For the even further increase in pileup, which is expected during data taking 2012, studies on MC samples simulated with higher pileup are needed.

5.7 PDF uncertainties on the acceptance

The method which has been used to estimate the PDF uncertainties is described in [41]. In general parton distribution functions (PDF) are measured quantities with uncertainties. PDFs provide the probability $F_i = F(x_i, Q)$ of finding a parton i with the longitudinal momentum fraction x and the momentum transfer Q in a proton or antiproton. The PDFs come into play when the cross-section of a process involving protons (Eq. 5.9) is calculated:

$$\frac{d\sigma}{dvariable}[pp \rightarrow X] \sim \sum_{ij} (f_{i/p}(x_1)f_{j/p}(x_2) + (i \leftrightarrow j))\hat{\sigma} \quad (5.9)$$

$\hat{\sigma}$ - cross section for the partonic subprocess $ij \rightarrow X$,

x_1x_2 - parton momentum fraction,

$f_{i/p}(x_i)$ - probability to find a parton i with momentum fraction x_i in the proton.

It is now necessary to understand how the PDF uncertainty contributes to the uncertainty of the probability of a process. The PDF uncertainties are obtained from a set of N Eigenvectors⁴ which have been orthogonalized with the Hessian Method. Each eigenvector probes a direction in the PDF parameter space that is a combination of the N free parameters used in a global fit on measured data. To calculate the uncertainty, the N eigenvectors have to be varied. Each eigenvector is varied up and down within tolerance to obtain $2N$ new parameter sets. By construction the variation in the direction of such eigenvectors is symmetric but this is not necessarily true when the uncertainties are propagated to the observable which depends on all N eigenvalues. To calculate the uncertainty the so called "Master Equation" [41] has been used:

$$\Delta X_{max}^+ = \sqrt{\sum_{i=1}^N [\max((X_i^+) - (X_0), (X_i^-) - (X_0, 0))]^2} \quad (5.10)$$

$$\Delta X_{max}^- = \sqrt{\sum_{i=1}^N [\max((X_0) - (X_i^+), (X_0, 0) - (X_i^-))]^2} \quad (5.11)$$

with X_i^\pm being the up and down variation of the i Eigenvector with the mean X_0 for the physical observable X . To obtain the PDF uncertainty on the acceptance the variation of the in and out of acceptance leptons needs to be calculated. This has been done according to the PDF4LHC recommendation with a tool provided by the Electroweak group [42]. The uncertainty for $t\bar{t}$ and W^\pm +jets events have been calculated separately because for the $t\bar{t}$ events a much higher uncertainty is expected since for the production gluon fusion is dominant where for W^\pm +jets, quark-quark interaction is mainly responsible. The gluon distribution in the proton can only be measured indirectly which results in bigger uncertainties compared to the direct measurable quark distribution [43]. The CTEQ66 PDF sets [44] were used to generate the studied MC samples (Sec. 4.3).

The resulting uncertainty on the acceptance efficiencies have been found to be 5.4% up and 4.7% down for the $t\bar{t}$ sample and 2.0% up and 2.1% down for the W^\pm +jets sample. Together with the uncertainty on the ratio between W^\pm +jets and $t\bar{t}$ events, discussed above (Sec. 5.8) a 6% uncertainty on the prediction has been applied.

⁴ $N = 20$ for CTEQ6 which has been used here

Table 5.5: The dominating systematic uncertainties of the lost-lepton prediction for the baseline selection.

#	Source	Systematic Uncertainties	
1	Statistics of the control-sample	+4.3%	−4.3%
2	iso-efficiencies (statistical, fit)	+5.6%	−4.1%
3	Differences $t\bar{t}$, W^\pm +jets, Z -samples and kinematic in control vs. signal region	+10.0%	−10.0%
4	Possible \cancel{E}_T dependency	+4.5%	−4.5%
5	SM background in control-region	+0%	−3.0%
6	MC use for acceptance calculation	+3.9%	−3.9%
7	transverse W-mass-cut	+4.6%	−4.0%
	total, combined systematics	+13.1%	−13.9%

5.8 Uncertainties

This section discusses how the most relevant uncertainties were found and justified. Tab. 5.5 includes all contribution that make up the total uncertainty for the baseline selection. The difference of the $t\bar{t}$, W^\pm +jets and Z sample, the SM background in the control-region, MC use for acceptance calculation and the m_T cut are constant for all search regions while the statistics of the CS, the isolation efficiencies and the possible \cancel{E}_T dependency are calculated for each region individually. The following enumeration corresponds to Tab. 5.5.

1. The most obvious uncertainty is the statistical uncertainty on the CS, $S_{CS} = \sqrt{\sum_i w_i}$ with S_{CS} being the statistical uncertainty and w_i the weight (calculated according to Eq.5.8 divided by CS) of each event in the CS.
2. The isolation efficiencies for electrons and muons have been measured by a Tag&Probe method (see Sec. 5.4.1) on a Z -sample where the Z decays leptonically. The uncertainty arising from the statistical limitation on this sample and the error due to the fitting procedure have been taken into account.
3. The electron and muon reconstruction efficiencies have been obtained from MC. The fraction of events including not reconstructed electrons and muons contribute 24% to the total background. An uncertainty of 9% on the total prediction has been found to be conservative by comparing the used MC efficiencies with the old Tag&Probe efficiencies. Together with other systematic uncertainties related to kinematic differences of the control- and signal region, as well as to remaining sample dependencies of the parametrized lepton efficiencies that are obtained on a Z -samples and applied to the $t\bar{t}$ and W^\pm +jets samples, an uncertainty of 10% is applied.
4. Fig. 5.14 shows the closure test for the \cancel{E}_T distribution of the not isolated muons (among other) for $t\bar{t}$ events (W^\pm +jets see Fig. 8.1). With increasing \cancel{E}_T an increasing under-prediction is being observed. As discussed in Sec. 5.4.4 the efficiency can not account for this. Fig. 5.19 shows the relative difference between Data-driven

Prediction from MC and MC expectation with a constant fit (red line) together with an blue error band which corresponds to the envelop of the the maximum of a linear fit ± 1 sigma error relative to the constant fit. The blue uncertainty band is taken as additional uncertainty on the prediction. The \cancel{E}_T selection for each exclusive search region determines the applied uncertainty. Tab. 5.6 shows these uncertainty for each \cancel{E}_T selection. This \cancel{E}_T dependency and possible others are treated as an additional uncertainty of up to 20% on the prediction.

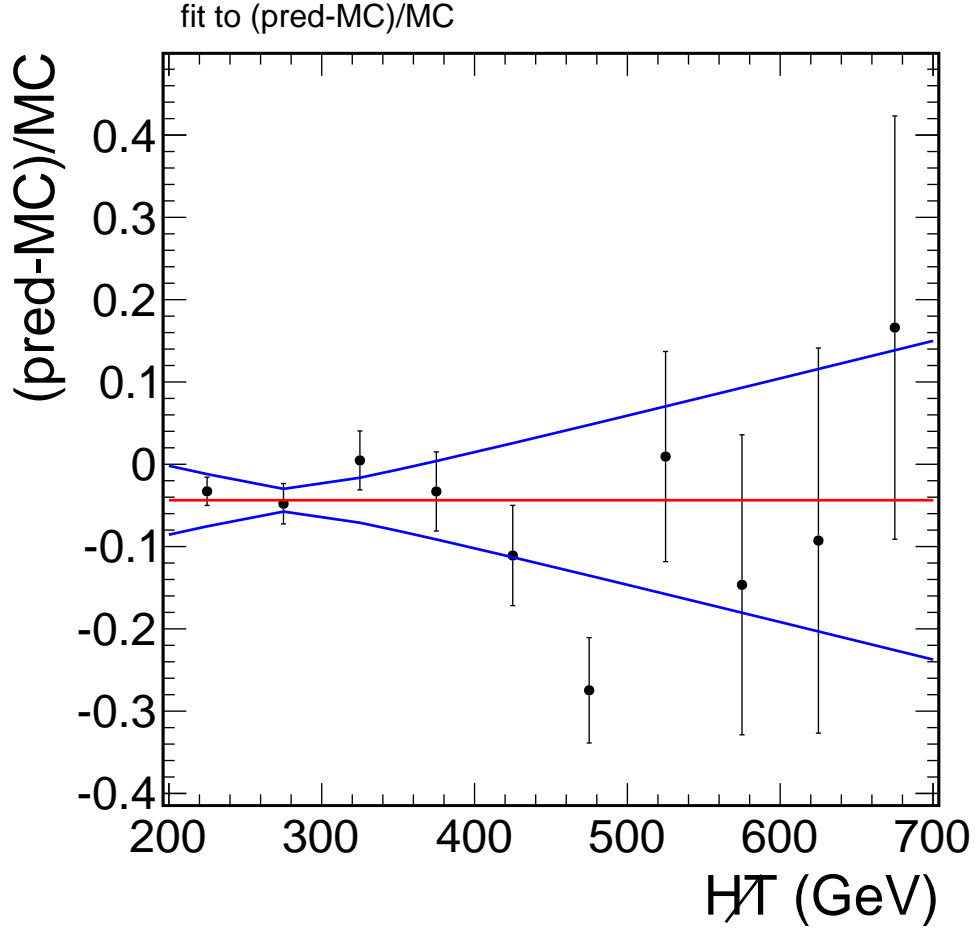


Figure 5.19: This plot shows the relative difference between Data-driven Prediction on MC and MC Expectation (dots with error band). Also a fit with a constant is shown (red). The blue lines show the ± 1 sigma envelope of a linear fit relative to the constant fit.

5. Background events from QCD, Z - or diboson events have been investigated by selecting a control sample on corresponding MC samples (see Sec. 5.2.2). Since only a very small number of events has been found to contribute a conservative uncertainty of 3% is adopted (see Sec. 5.2.2).

6. The corrections for out-of-acceptance leptons have been taken from MC. The uncertainty on the acceptance efficiency is found to be smaller than 9% leading to a total uncertainty of about 6% on the prediction. This value covers the PDF uncertainty discussed in greater detail in Sec. 5.7 and the uncertainty on the different contribution of the $t\bar{t}$ and W^\pm +jets sample.
7. A minor contribution to the total statistical uncertainty arises from the correction due to the transverse mass cut discussed in Sec. 5.2.1. This uncertainty can be divided into three parts:
 - The \cancel{E}_T scale dependence, which has been determined by observing the variation of the correction factor while varying the \cancel{E}_T by 10%,
 - a conservative assumption on the uncertainty due to \cancel{E}_T outliers⁵,
 - and an uncertainty on the fraction of dileptonic $t\bar{t}$ events which has been obtained from MC.

The correction factor with the combined uncertainty is calculated to be $10\% \pm 4\%$. Studies have been performed (see Sec. 5.2.1) on the efficiency of the m_T cut for each search region. The variation of the mean of the efficiency is within the 40% assigned uncertainty.

Table 5.6: This table contains the uncertainty assigned according to the \cancel{E}_T selection of each region due to \cancel{E}_T decency of the prediction.

\cancel{E}_T (GeV)	Pred.
200 ... 350	4.6%
200 ...	8.2%
350 ... 500	8.2%
350 ...	8.2%
500 ... 600	13.3%
500 ...	16.4%
600 ...	20.0%

⁵ \cancel{E}_T outliers arise when

6 Combination of other backgrounds with the lost lepton and result interpretation

This section focuses on the other background estimations contributing to the jets and missing transverse momentum analysis introduced in Sec. 4, comparison of the prediction of all background estimations to the selected events on the 4.98 fb^{-1} collected by the CMS detector in 2011 (Sec. 6.1) and the interpretation of the results in the cMSSM (Sec. 6.2.1) and Simplified models (Sec. 6.2.2). The obtained exclusion limits in the cMSSM are among the most sensitive limits world wide. The results have been approved by the CMS collaboration [45] and will be published. All plots in this section labeled "CMS Simulation", "CMS preliminary" or "CMS" can be found on the public twiki web page [38]. It is worth pointing out that the analyses has not been designed specifically for the above mentioned SUSY Models which makes it capable of detecting a much wider range of new particles which are strangely produced, decaying to a weakly interaction particle in the final state. The cMSSM and the Simplified Models are used to demonstrate the power of this analysis.

The other background predictions, results and limits are described in greater detail in the Analysis Note [2].

6.0.1 The QCD background estimation

One background especially important for high H_T search regions is the background arising from mismeasured jets leading to artificial \cancel{H}_T in QCD multi-jet events.

This background is estimated using data events collected by mostly prescaled H_T triggers¹. These data also include the electroweak contribution passing the lepton veto and any potential new physics events². The estimation of QCD events has been done by a so called "Rebalance and Smear" method [2] which can be seen as a sketch in Fig. 6.1

This method involves the following steps: First, jets with $p_T > 15 \text{ GeV}$ in an event are balanced in the transverse plane, using a kinematic fit. When a prescaled trigger is used to collect the events they have to be smeared N times according to the jet response function³, in order to reduce statistical uncertainties. The non-Gaussian tale of the jet response function are very important for the high H_T and \cancel{H}_T regions. Much work has been done to model these tails precisely.

This procedure is repeated 100 times. The mean and variance of the resulting predictions is calculated and used for the QCD background estimation.

The main uncertainties on the QCD background estimation arises from non-closure, the shape of the jet response functions including the Gaussian width, the tails, the heavy flavor

¹Prescaled triggers collect only every N events that meets the trigger requirements to reduce the otherwise too high data rate to be recorded.

²Note, their cross section is negligible compared to the QCD multi jet cross section.

³The jet response function describes the mis-measurement of jets and has been obtained from simulation and has been corrected for the differences to data

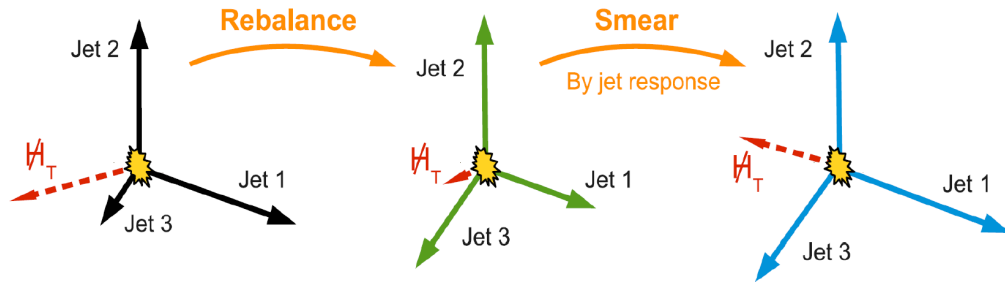


Figure 6.1: This sketch illustrates the Rebalance and Smear method used to estimate the QCD background contribution [2].

contribution, and the effect of pileup on jet measurements. The resulting total uncertainty adds up to 60 – 70%.

The QCD method is extremely important since it is dominant for one of the most sensitive search regions (the $H_T > 1400$, $\cancel{H}_T > 200$ region).

In addition a factorization method has been used for cross checks. Both methods lead to comparable results as can be seen in greater detail in the AN [2].

6.0.2 The Z to invisible background estimation

The background arising from events including jets and a Z -Boson which decays to two neutrinos has been evaluated with two methods [2].

The $Z \rightarrow \nu\nu$ background is estimated by removing the γ in a γ +jets data sample and

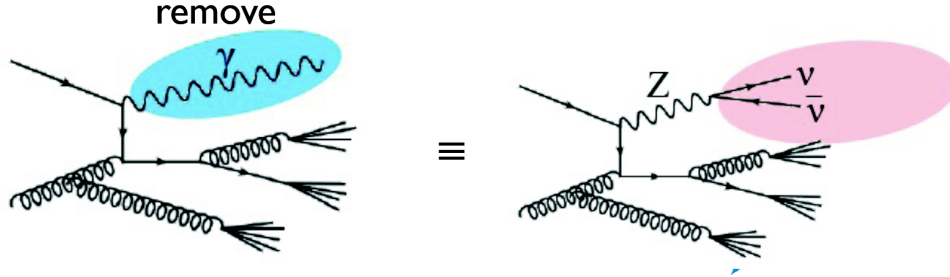


Figure 6.2: This sketch illustrates the γ +jets method used for the $Z \rightarrow \nu\nu$ background estimation.

correcting for the differences between the γ and the $Z \rightarrow \nu\nu$ process. The Z boson and photon exhibit similar kinematic properties at high boson p_T . Also the hadronic component of these events is similar. A γ +jets sample is corrected for the γ reconstruction efficiency and the photon purity. Both are measured from data and the $Z(\nu\bar{\nu})$ +jets/ γ +jets ratio, from simulation, which includes the modeling of the production and acceptance. Fig. 6.2 illustrates the basic idea of removing the γ from the sample to model the $Z^0 \rightarrow \nu\nu$ events.

The resulting total correction factor is 0.28 ± 0.06 for the baseline selection. The theoretical uncertainty because of EWK [2], leading log on the γ - Z cross-section ratio of 21 – 42% is the dominate systematic uncertainty. Also the detector acceptance of $\pm 5\%$, the photon reconstruction efficiency and the purity of the photon sample contribute.

For a cross check a second method is used, which starts with jets and $Z \rightarrow \mu\mu$ sample. The muons are removed and the branching ratio of $R(Z \rightarrow \nu\nu/Z \rightarrow \mu\mu)$ is applied.

The prediction for the baseline selection of 602 ± 100 events agrees well with the 595 ± 135 events predicted from the γ +jets method.

6.0.3 The hadronic τ background estimation

One part of the $t\bar{t}$ and W^\pm +jets events can decay to a τ further decaying hadronically. This background is estimated by selecting a muon control sample similar to the control sample used for the lost-lepton estimation. Instead of a H_T - \cancel{H}_T cross trigger an inclusive μ or a μ trigger with at least two jets is used with exactly one μ with $p_T > 20$ GeV and $|\eta| < 2.1$.

The background is estimated by replacing the muon p_T by a jet p_T taken from a simulated response function for a hadronically-decaying τ which can be seen in Fig. 6.3. The H_T and \cancel{H}_T distribution is recalculated including the τ -jet, and the search selections are applied to predict the hadronic- τ background.

The τ -jet response template is parametrized in p_T^{jet}/p_T^τ and is obtained from $t\bar{t}$ and

$W^\pm + \text{jets}$ MC events by matching a reconstructed τ -jet with the corresponding generated τ . In addition corrections have been applied to account for the trigger efficiency, acceptance and efficiency of the μ selection, and the relative branching ratio of $R(W \rightarrow \tau\nu(\tau \rightarrow \text{hadrons})/(W \rightarrow \mu\nu)) = 0.69 \pm 0.05$.

The main systematic uncertainties arise from the uncertainty on the correction and additional up to 11% uncertainty based on non closure and the MC statistics used. In addition systematic uncertainties arise from the μ acceptance ($\leq 13\%$), the τ -jet response function ($\leq 20\%$), and the subtraction of residual QCD multi jet and $Z \rightarrow \mu\mu$ events.

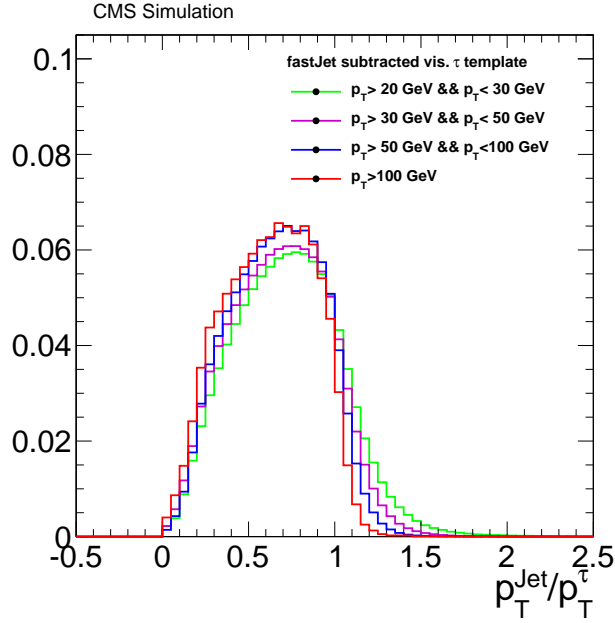


Figure 6.3: This figure shows a typical hadronic τ response template used for the background estimation [2].

6.1 Combination of all backgrounds

The combination of all the background estimations and the selection on the full 4.98 fb^{-1} luminosity can be seen in Tab. 6.1. All the background estimations are also shown in Fig. 6.4 for the full baseline selection and Fig. 6.5 for each search region separately. Very good agreement for the H_T and \cancel{H}_T distribution can be observed. No significant excess above the combined prediction can be observed. This result is interpreted in terms of limits within the cMSSM and Simplified Models in the next section.

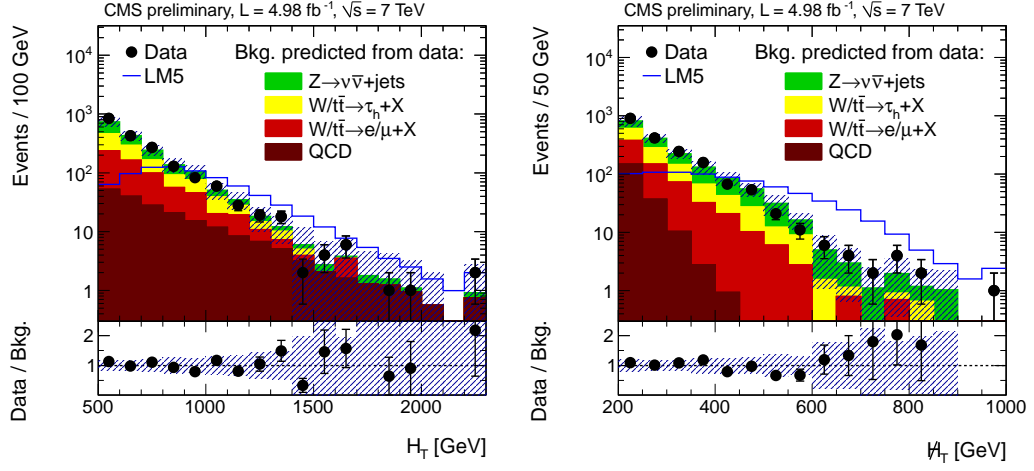


Figure 6.4: H_T (left) and H_T (right) distributions in data compared to the combined data-driven background predictions and to the SUSY LM5 benchmark scenario. The ratio of the selection on data to the combined data-driven background predictions can be found on the bottom. The hatched area represents the combined systematic and statistical uncertainties on the prediction [2].

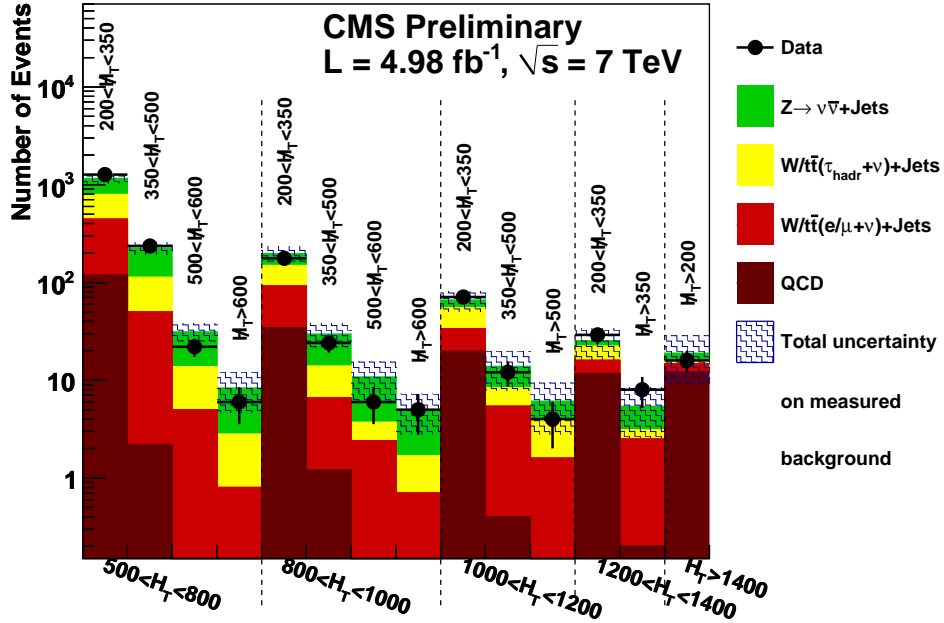


Figure 6.5: Summary of backgrounds estimated from data and observed events in data for 14 search regions used in the analysis and presented in Tab. 6.1 [2]

Table 6.1: Predicted event yields from the different background estimation methods for the baseline selection and for the search selections using 4.98 fb^{-1} dataset. An additional row with total is added where statistical uncertainties are treated uncorrelated and systematic uncertainties are added assuming full correlation.

Selection		$z\nu\nu$ from $\gamma+\text{jets}$	$t\bar{t}/W^\pm$ $\rightarrow e, \mu+X$	$t\bar{t}/W^\pm$ $\rightarrow \tau_{\text{had}\tau}+X$	QCD	Total background	Observed in data
HT	MHT						
500-800	200-350	359.2 ± 82.2	326.5 ± 47.0	348.5 ± 40.1	118.6 ± 76.9	1152.9 ± 128.4	1269
500-800	350-500	112.3 ± 27.4	47.8 ± 9.2	62.5 ± 8.7	2.2 ± 2.2	224.8 ± 30.3	236
500-800	500-600	17.6 ± 5.6	5.0 ± 2.2	8.7 ± 2.5	0.0 ± 0.1	31.3 ± 6.5	22
500-800	>600	5.5 ± 3.1	0.8 ± 0.8	2.0 ± 1.8	0.0 ± 0.0	8.3 ± 3.6	6
800-1000	200-350	48.4 ± 19.1	57.7 ± 15.3	56.3 ± 8.3	34.6 ± 24.0	197.0 ± 35.3	177
800-1000	350-500	16.0 ± 7.3	5.4 ± 2.3	7.2 ± 2.0	1.2 ± 1.3	29.8 ± 8.0	24
800-1000	500-600	7.1 ± 4.5	2.4 ± 1.5	1.3 ± 0.6	0.0 ± 0.2	10.8 ± 4.8	6
800-1000	>600	3.3 ± 2.0	0.7 ± 0.7	1.0 ± 0.3	0.0 ± 0.1	5.0 ± 2.2	5
1000-1200	200-350	10.9 ± 5.5	13.7 ± 3.8	21.9 ± 4.6	19.7 ± 13.3	66.2 ± 15.5	71
1000-1200	350-500	5.5 ± 3.5	5.0 ± 4.4	2.9 ± 1.3	0.4 ± 0.7	13.7 ± 5.8	12
1000-1200	>500	2.2 ± 2.9	1.6 ± 1.2	2.3 ± 1.0	0.0 ± 0.2	6.1 ± 3.3	4
1200-1400	200-350	3.1 ± 2.0	4.2 ± 2.1	6.2 ± 1.8	11.7 ± 8.3	25.1 ± 9.0	29
1200-1400	>350	2.3 ± 2.3	2.3 ± 1.4	0.6 ± 0.8	0.2 ± 0.6	5.5 ± 2.9	8
>1400	>200	3.2 ± 2.4	2.7 ± 1.6	1.1 ± 0.5	12.0 ± 9.1	18.9 ± 9.6	16
Baseline		596.6 ± 165.0	475.8 ± 76.2	522.4 ± 67.0	200.7 ± 82.7	1795.4 ± 205.9	1885

6.2 Interpretation of the results

The results are interpreted by setting limits with a 95% confidence level (CL) with the CLs method [46] [47] within the cMSSM and simplified models.

The CLs is a ratio of confidence levels $CL_s = \frac{CL_{s+b}}{CL_b}$ ⁴ designed to obtain the best limits while avoiding excluding signals, to which the analysis is not really sensitive to. The confidence in a specific hypothesis x is given by the probability that the test-statistic Q being the likelihood ratio [45] is less than or equal to the observed value in the data Q_{obs} :

$$CL_x = P_x(Q \leq Q_{obs}). \quad (6.1)$$

Each of the 14 bins in H_T and \cancel{H}_T as summarized in Tab. 6.1 are used as statistically independent channels in the limit calculation. The used test-statistic Q is constructed using the product of the individual likelihoods per channel. The correlation of the systematic uncertainties among different bins is taken into account. Especially the similarity of the isolated muon control sample used for the lost-lepton and for the hadronic-tau background estimation methods are taken as correlated into account.

6.2.1 Interpretation within the cMSSM

As discussed in Sec. 2.3.1 the CMSSM has only five independent parameters. The signal cross section is calculated at NLO using PROSPINO [48]. For the LM5⁵ benchmark point the H_T and \cancel{H}_T signal are shown in Fig. 6.4.

The limits are calculated for the $m_0, m_{1/2}$ plane and are translated to the m_g, m_q plane while the other parameters are fixed to $A_0 = 0, \tan\beta = 10$, and $\text{sign}(\mu) > 0$.

From cMSSM signal samples the efficiency of the event selection for each different parameter set of $m_0, m_{1/2}$ is evaluated. This expected event selection efficiency is used to set limits with the CL_s method.

The uncertainty on the efficiency of the event selection takes the statistical component, the jet energy scale, the jet energy resolution, PDF uncertainties, the uncertainty on the luminosity, trigger inefficiency and inefficiency due to event cleaning into account. Fig. 6.6 shows the observed limit together with the expected and the ± 1 sigma uncertainty band for the $m_0, m_{1/2}$ and for the m_g, m_q . The dashed line with the yellow band shows the expected limit together with the ± 1 sigma uncertainty band. Everything below the observed limit is excluded at 95% confidence level. For comparison the limit obtained with the same methods on data from 2010 corresponding to 36pb^{-1} are shown. The increased statistics lead to a much larger excluded region.

⁴where CL_{s+b} is the confidence in the signal+background hypothesis, and CL_b is the confidence in the background-only hypothesis.

⁵ $m_0 = 230 \text{ GeV}, m_{1/2} = 360 \text{ GeV}, A_0 = 0, \tan\beta = 10$, and $\text{sign}(\mu) > 0$

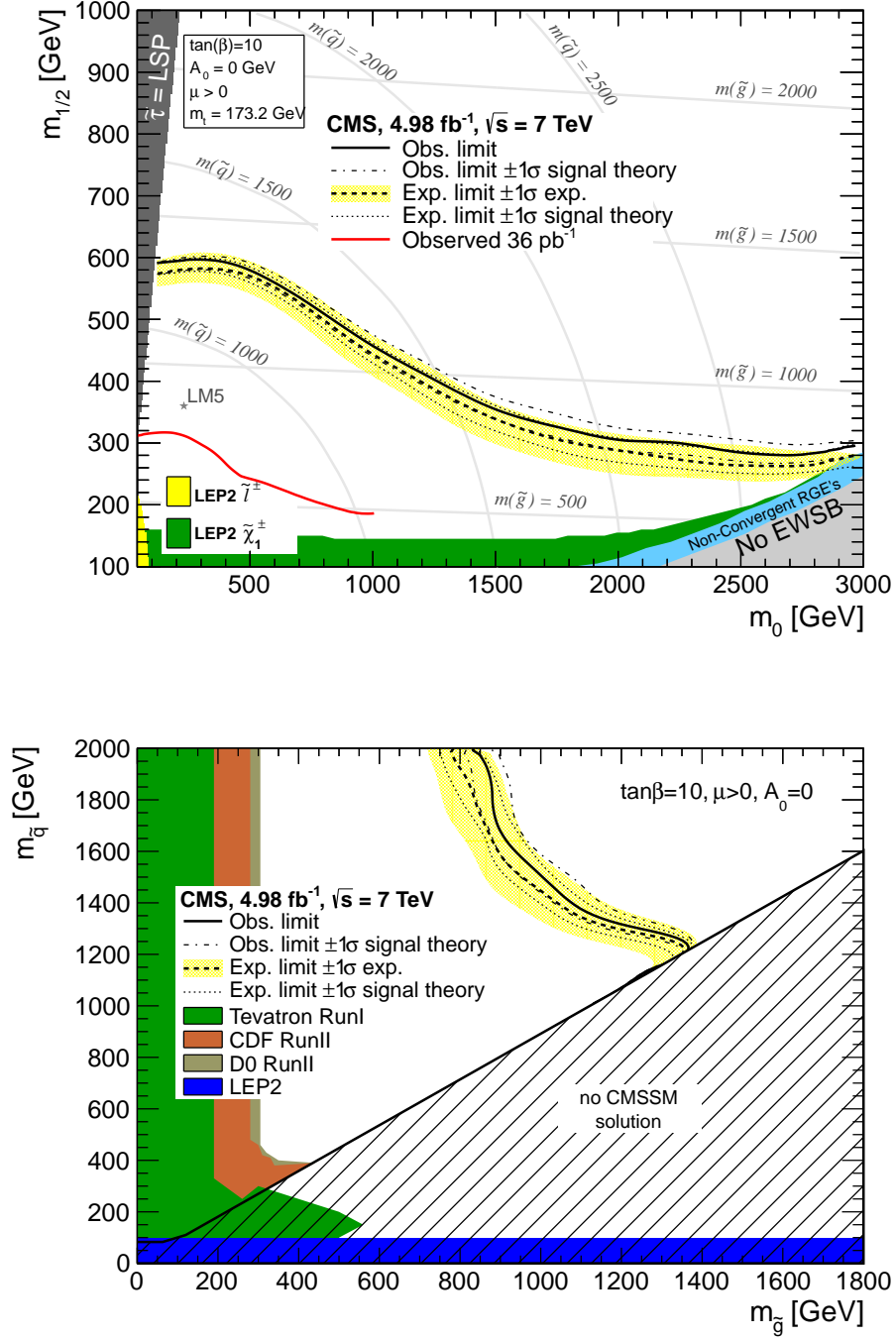


Figure 6.6: Both plots shows the interpretation of the results within the cMSSM model for the $m_0, m_{1/2}$ plane on top and the same limits translated to the $m_{\tilde{g}}, m_{\tilde{q}}$ plane on bottom. Everything below the observed limit (black line) is excluded at 95% CL. The dashed line with the yellow band shows the expected limit together with the ± 1 sigma uncertainty band.

6.2.2 Interpretation with Simplified Model Spectra

The results of the analysis are also interpreted within the Simplified Model Spectra (SMS). The results are interpreted in two benchmark simplified models:

- pair-produced gluinos, where each gluino decays directly to two lighter quarks and the LSP
- pair-produced squarks, where each squark decays to one gluon or quark and the LSP

In Fig. 6.7 the respective diagrams for these simplified models are presented. The role

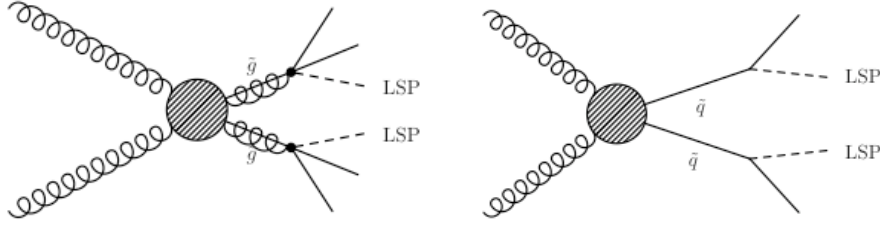


Figure 6.7: Feynman diagram of simplified models. Left: gluino pair production; right: squark pair production.

of simplified models is to represent observable processes. Several topologies are chosen that can bracket the kinematics of the different final states. For each topology several masses are generated for each of the particles involved. This way more mass splittings can be explored than in the cMSSM where the ratio of the gluino and the LSP masses is approximately fixed. In the case of limit derivation, it is useful to have a reference cross section to compare results between analyses and experiments.

The cross-section limits for the gluino pair production (topology T1) and squark pair production (topology T2) are shown in Fig. 6.8.

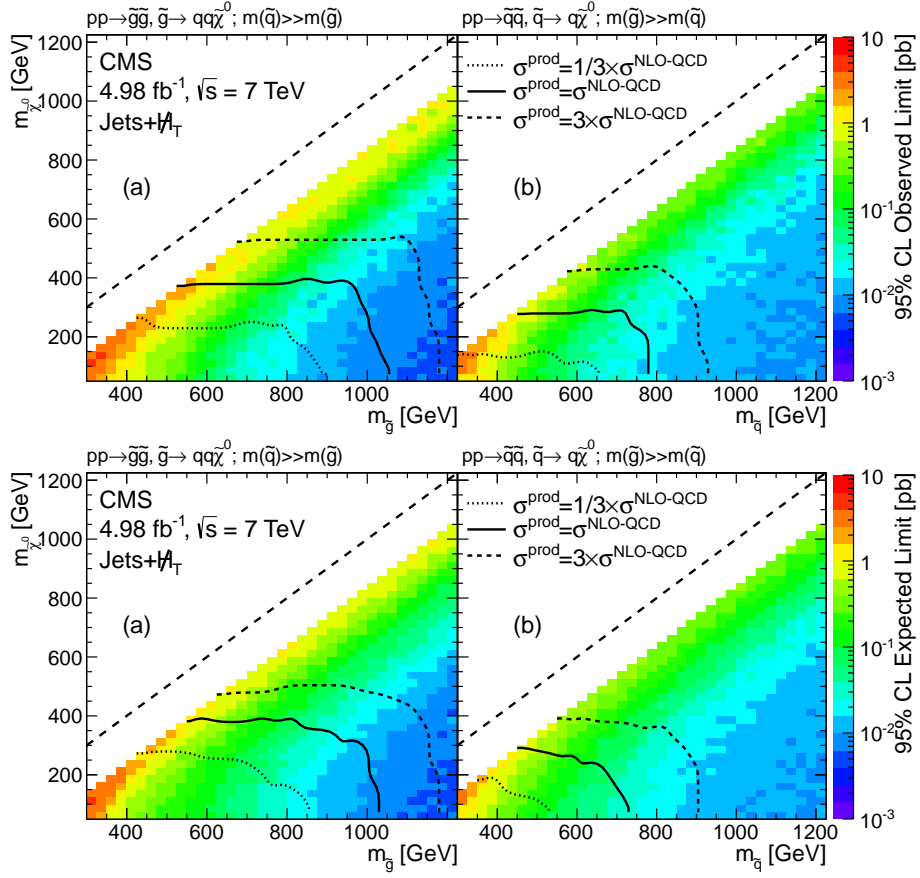


Figure 6.8: (Top) **Observed** and (Bottom) **Expected 95% C.L. exclusion limits** for the (a) gluino pair production (topology T1), and (b) squark pair production (topology T2).

7 Conclusion and outlook

In this thesis a method has been presented which is able to predict events including high energetic jets and undetected leptons from a W -decay in the final state. A muon control sample is selected on data and reweighted to predict the undetected leptons using reconstruction and isolation efficiencies obtained from MC and with a Tag & Probe method on data. The method has been improved in the context of higher pileup, more statistics and with increased H_T and \cancel{H}_T cuts. Tests have been performed to prove that the method is capable of estimating the background for very high pileup distributions and very high H_T and \cancel{H}_T selections. These studies show that the method can be applied for the even higher pileup and H_T and \cancel{H}_T cuts as expected for the 2012 data.

The method has been used together with the other background estimations in a search for events hinting to physics beyond the SM on the 4.98 fb^{-1} of data collected by CMS in 2011. Since no excess over SM expectations has been observed, limits have been calculated in the cMSSM and Simplified models excluding first and second generation squark and gluino masses up to $\tilde{q} \approx 1.2 \text{ GeV}$ and $\tilde{g} \approx 650 \text{ GeV}$. These limits are among the world wide most sensitive limits published up to date.

The increased center of mass energy in 2012 of $\sqrt{s} = 8 \text{ TeV}$ and the expected 14 TeV in 2014 will improve the sensitivity of this analyses even further in the higher $m_0, m_{1/2}$ plane of the cMSSM and also for the Simplified Models.

Another focus has recently become increasingly important. The exclusion of a very large fraction of the $m_0, m_{1/2}$ plane for first and second generation squarks suggests to focus on the search for third generation squarks. Third generation squark decays include often a b-jet motivating the implementation of a b-tag in order to select two independent samples one with a b-tag one without which would increase the sensitivity of this analysis.

Despite the fact that a large space in the cMSSM model framework has been excluded the search for physics beyond the SM will continue and especially for the more challenging search for third generation squarks the hunt is far from over.

8 Appendix

In this part the additional closure plots are shown.

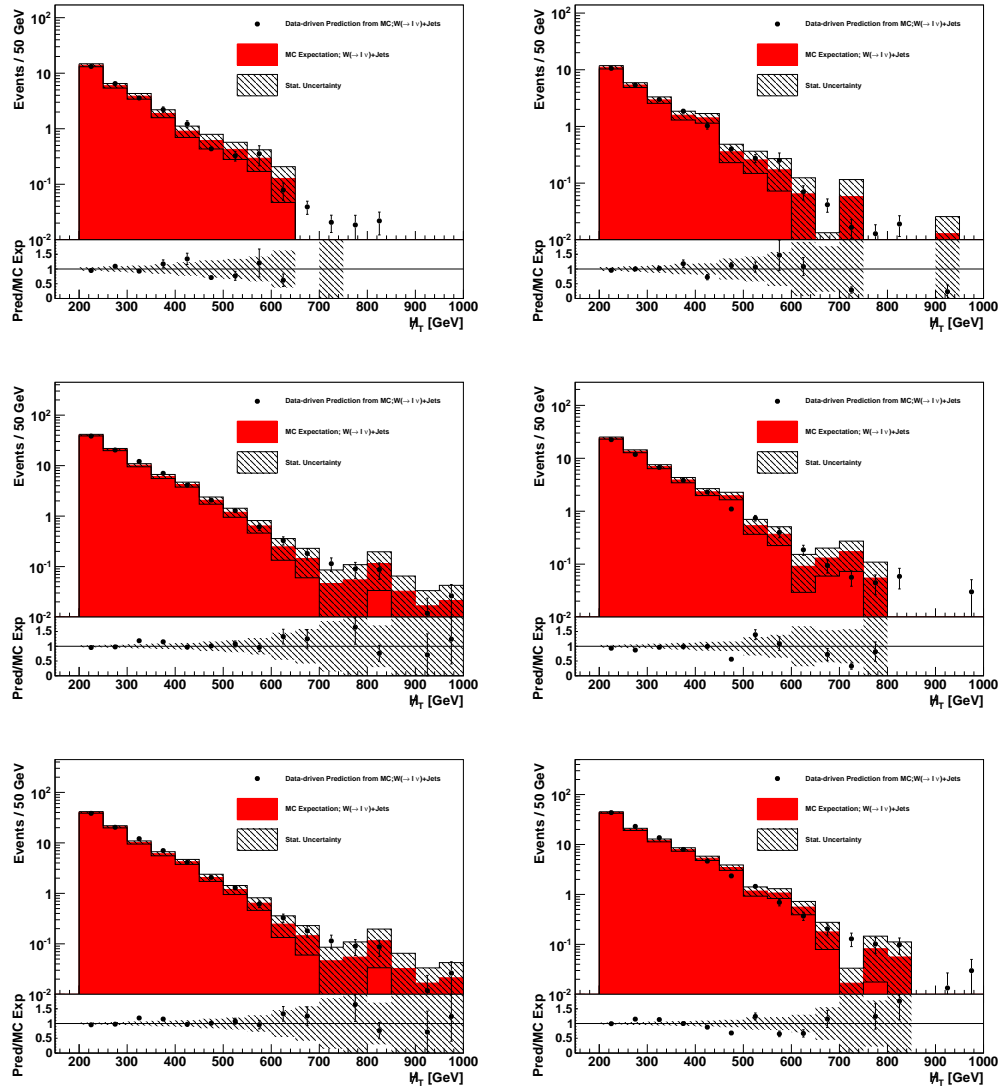


Figure 8.1: This plots show the closure tests for $W^\pm + \text{jets}$ separated for the not isolated (top), not reconstructed and out of acceptance fraction for muons (left) and electrons (right). Good agreement for the shape can be observed. The legend description can be found in the caption of Fig. 5.12.

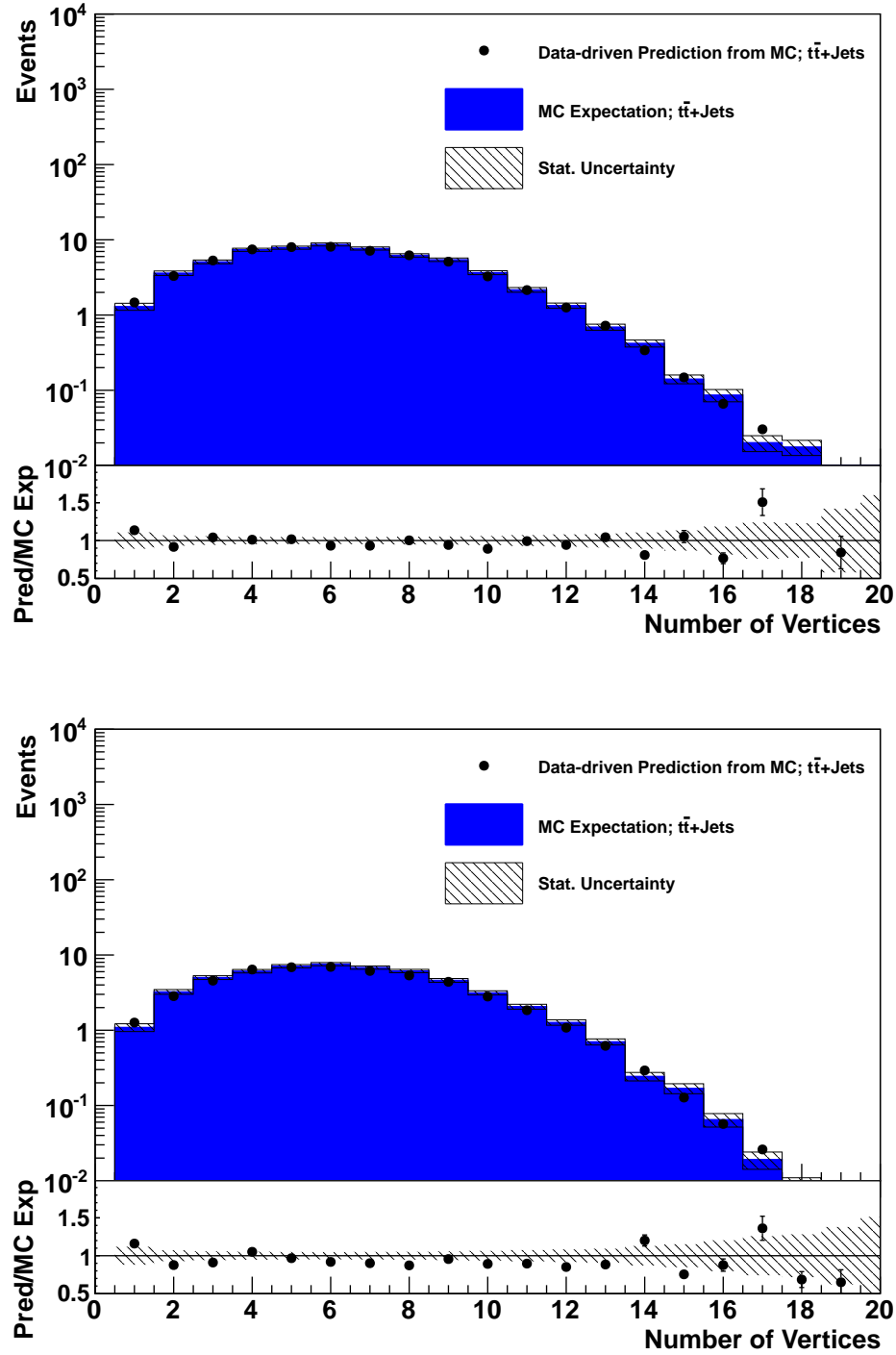


Figure 8.2: These plots show the closure tests for the out of acceptance electrons (top) and muons (bottom) for $t\bar{t}$, as the number of vertices. The legend description can be found in the caption of Fig. 5.12.

Bibliography

- [1] Tevatron, “TeVatron Feynman Diagrams”.
- [2] CMS, “Inclusive search for new physics at CMS with the jets and missing momentum signature”,.
- [3] ATLAS Collaboration, “An update to the combined search for the Standard Model Higgs boson with the ATLAS detector at the LHC using up to 4.9 fb^{-1} of pp collision data at $\sqrt{s} = 7 \text{ TeV}$ ”, *ATLAS Note* **ATLAS-CONF-2012-019** (2012).
- [4] CMS Collaboration, “Combination of SM, SM4, FP Higgs boson searches”, *CMS Physics Analysis Summary* **CMS-PAS-HIG-12-008** (2012).
- [5] TEVNPH (Tevatron New Phenomina and Higgs Working Group), CDF and D0 Collaborations, “Combined CDF and D0 Upper Limits on Standard Model Higgs Boson Production with up to 8.6 fb^{-1} of Data”, [arXiv:1107.5518](#). 2011. CDF Note 10606. D0 Note 6226. FERMILAB-CONF-11-354-E. Submitted to the EPS 2011 Conference.
- [6] P. Schmüser, “Feynman-Graphen und Eichtheorien für Experimentalphysiker”. Lecture Notes in Physics. Springer, Berlin, Heidelberg, New York, London, Paris, Tokyo, 1988. ISBN 0-387-18797-9.
- [7] The ALEPH, DELPHI, L3, OPAL, SLD Collaborations, the LEP Electroweak Working Group, the SLD Electroweak and Heavy Flavour Groups, “Precision Electroweak Measurements on the Z Resonance”, *Phys. Rept.* **427** (2006) 257, [arXiv:hep-ex/0509008](#).
- [8] H1 and ZEUS Collaboration, “Combined Measurement and QCD Analysis of the Inclusive $e^{\pm}p$ Scattering Cross Sections at HERA”, *JHEP* **01** (2010) 109, [arXiv:0911.0884](#). [doi:10.1007/JHEP01\(2010\)109](#).
- [9] P. W. Higgs, “Broken Symmetries and the Masses of Gauge Bosons”, *Phys. Rev. Lett.* **13** (1964) 508 – 509. [doi:10.1103/PhysRevLett.13.508](#).
- [10] G. Bertone, D. Hooper, and J. Silk, “Particle dark matter: evidence, candidates and constraints”, *Physics Reports* **405** (2005), no. 5-6, 279 – 390. [doi:10.1016/j.physrep.2004.08.031](#).
- [11] I. Aitchison, “Supersymmetry in Particle Physics – An Elementary Introduction”. Cambridge University Press, 2007. ISBN 978-0-521-88023-7.
- [12] SNO Collaboration Collaboration, “Constraints on nucleon decay via ‘invisible’ modes from the Sudbury Neutrino Observatory”, *Phys.Rev.Lett.* **92** (2004) 102004, [arXiv:hep-ex/0310030](#). [doi:10.1103/PhysRevLett.92.102004](#).

- [13] Super-Kamiokande Collaboration, “Search for Proton Decay via $p \rightarrow e^+\pi^0$ and $p \rightarrow \mu^+\pi^0$ in a Large Water Cherenkov Detector”, *Phys. Rev. Lett.* **102** (2009) 141801. doi:10.1103/PhysRevLett.102.141801.
- [14] D0 Collaboration, Abazov et al., “Search for squarks and gluinos in events with jets and missing transverse energy using 2.1 fb^{-1} of $p\bar{p}$ collision data at $\sqrt{s} = 1.96\text{ TeV}$ ”, *Phys. Lett. B* **660** (2008) 449, arXiv:0712.3805.
- [15] CDF Collaboration, Altonen et al., “The CDF exclusion region in the $m_{1/2}$ vs. m_0 plane”, *Phys. Rev. Lett* **102** (2009) 121801, arXiv:011.2512.
- [16] L3 Collaboration, “Search for Scalar Leptons and Scalar Quarks at LEP”, *Phys. Lett. B* **580** (2004) 37, arXiv:hep-ex/0310007. See also references therein. doi:10.1016/j.physletb.2003.10.010.
- [17] L. Evans and P. Bryant, “LHC Machine”, *Journal of Instrumentation* **3** (2008), no. 08, S08001. doi:10.1088/1748-0221/3/08/S08001.
- [18] O. S. Brüning, P. Collier, P. Lebrun et al., “LHC Design Report”, volume 1: The LHC Main Ring. CERN, Geneva, 2004. CERN-2004-003-V-1.
- [19] M. Lamont, “The LHC from Commissioning to Operation”, in *Proceedings of the 2nd International Particle Accelerator Conference IPAC11*, C. Petit-Jean-Genaz, ed., pp. 11 – 15. San Sebastián, Spain, 2011. <http://www.jacow.org/>.
- [20] ATLAS Collaboration, “The ATLAS Experiment at the CERN Large Hadron Collider”, *JINST* **3** (2008) S08003. doi:10.1088/1748-0221/3/08/S08003.
- [21] CMS Collaboration, “CMS Detector Performance and Software”, volume 1 of *CMS Physics Technical Design Report*. CERN, Geneva, 2006. CMS-TDR-008-1. CERN-LHCC-2006-001.
- [22] LHCb Collaboration, “The LHCb Detector at the LHC”, *JINST* **3** (2008) S08005. doi:10.1088/1748-0221/3/08/S08005.
- [23] ALICE Collaboration, “The ALICE experiment at the CERN LHC”, *JINST* **3** (2008) S08002. doi:10.1088/1748-0221/3/08/S08002.
- [24] CMS Collaboration, “Absolute Calibration of Luminosity Measurement at CMS: Summer 2011 Update”, *CMS Physics Analysis Summary CMS-PAS-EWK-11-001* (2011).
- [25] CMS Collaboration, “The CMS experiment at the CERN LHC”, *JINST* **3** (2008) S08004. doi:10.1088/1748-0221/3/08/S08004.
- [26] CMS Collaboration, “The CMS tracker system project”, volume 5 of *Technical Design Report CMS*. CERN, Geneva, 1997. CMS-TDR-005. CERN-LHCC-98-006.
- [27] CMS Collaboration, “Tracking and Primary Vertex Results in First 7 TeV Collisions”, *CMS Physics Analysis Summary CMS-PAS-TRK-10-005* (2010).

- [28] CMS Collaboration, “The CMS electromagnetic calorimeter project”, volume 4 of *Technical Design Report CMS*. CERN, Geneva, 1997. CMS-TDR-004. CERN-LHCC-97-033.
- [29] CMS Collaboration, “The CMS hadron calorimeter project”, volume 2 of *Technical Design Report CMS*. CERN, Geneva, 1997. CMS-TDR-002. CERN-LHCC-97-031.
- [30] CMS Collaboration, “The CMS muon project”, volume 3 of *Technical Design Report CMS*. CERN, Geneva, 1997. CMS-TDR-003. CERN-LHCC-97-032.
- [31] CMS Collaboration, “CMS TriDAS project: the trigger system”, volume 6 of *Technical Design Report CMS*. CERN, Geneva, 2000. CMS-TDR-006-1. CERN-LHCC-2000-038.
- [32] B. Dahmes, “Triggers for LHC Physics”, 2011. Lecture at CERN Summer Student Programme.
- [33] CMS Collaboration, “Photon reconstruction and identification at $\sqrt{s} = 7$ TeV”, *CMS Physics Analysis Summary CMS-PAS-EGM-10-005* (2010).
- [34] CMS Collaboration, “Electron reconstruction and identification at $\sqrt{s} = 7$ TeV”, *CMS Physics Analysis Summary CMS-PAS-EGM-10-004* (2010).
- [35] CMS Collaboration, “Performance of muon identification in pp collisions at $\sqrt{s} = 7$ TeV”, *CMS Physics Analysis Summary CMS-PAS-MUO-10-002* (2010).
- [36] CMS Collaboration, “Particle-Flow Event Reconstruction in CMS and Performance for Jets, Taus, and E_T^{miss} ”, *CMS Physics Analysis Summary CMS-PAS-PFT-09-001* (2009).
- [37] CMS Collaboration, “Determination of Jet Energy Calibration and Transverse Momentum Resolution in CMS”, *Journal of Instrumentation* **6** (2011) P11002, [arXiv:1107.4277](https://arxiv.org/abs/1107.4277). doi:10.1088/1748-0221/6/11/P11002.
- [38] CMS Collaboration, “Search for new physics in the multijets + missing transverse energy final state in 7 TeV proton-proton collisions”, *CMS Wiki* (2012). <https://twiki.cern.ch/twiki/bin/view/CMSPublic/PhysicsResultsSUS12011>, Topic revision: r2.
- [39] C. Berger, “Elementarteilchenphysik: Von den Grundlagen zu den modernen Experimenten”. Springer-Lehrbuch. Springer, Berlin, Heidelberg, New York, 2002. ISBN 3-540-41515-7.
- [40] J. Thomsen, “Search for Supersymmetry in the Hadronic Channel with Data from the CMS Experiment”. PhD thesis, Universität Hamburg, Hamburg, Germany, 2012.
- [41] D. Bourilkov, R. C. Group, and M. R. Whalley, “LHAPDF: PDF use from the Tevatron to the LHC”, [arXiv:hep-ph/0605240](https://arxiv.org/abs/hep-ph/0605240).
- [42] E. groupe CMS, “Electroweak utilities for MC corrections and systematics evaluation”.

- [43] H1 and ZEUS Collaboration, “Combined Measurement and QCD Analysis of the Inclusive $e^\pm p$ Scattering Cross Sections at HERA”, *JHEP* **1001** (2010) 109, [arXiv:0911.0884](#). [doi:10.1007/JHEP01\(2010\)109](#).
- [44] CTEQ Collaboration, “The Coordinated Theoretical-Experimental Project on QCD”, 2011. <http://cteq.org>.
- [45] CMS Collaboration, “Search for supersymmetry in all-hadronic events with missing energy”, *CMS Physics Analysis Summary* **CMS-PAS-SUS-11-004** (2011).
- [46] A. L. Read, “Presentation of search results: the CL_s technique”, *Journal of Physics G: Nuclear and Particle Physics* **28** (2002), no. 10, 2693 – 2704. [doi:10.1088/0954-3899/28/10/313](#).
- [47] T. Junk, “Confidence level computation for combining searches with small statistics”, *Nuclear Instruments and Methods in Physics Research Section A: Accelerators, Spectrometers, Detectors and Associated Equipment* **434** (1999), no. 2-3, 435 – 443. [doi:10.1016/S0168-9002\(99\)00498-2](#).
- [48] W. Beenakker, R. Hopker, and M. Spira, “PROSPINO: A Program for the production of supersymmetric particles in next-to-leading order QCD”, [arXiv:hep-ph/9611232](#).